Path Delays in the Neutral Atmosphere

Tobias Nilsson, Johannes Böhm, Dudy D. Wijaya, Ana Tresch, Vahab Nafisi and Harald Schuh

Abstract This part describes the effects of the troposphere—strictly speaking the neutral atmosphere—on the propagation delay of space geodetic signals. A theoretical description of this tropospheric propagation delay is given as well as strategies for correcting for it in the data analysis of the space geodetic observations. The differences between the tropospheric effects for microwave techniques, like the

T. Nilsson (✉)
Section 1.1 GPS/Galileo Earth Observations, Helmholtz Centre Potsdam GFZ German Research Centre for Geosciences,
Telegrafenberg A 17, 14473 Potsdam, Germany
e-mail: nilsson@gfz-potsdam.de

J. Böhm
Department of Geodesy and Geoinformation, Vienna University of Technology,
Gußhausstraße 27-29, 1040 Vienna, Austria
e-mail: johannes.boehm@tuwien.ac.at

D. D. Wijaya
Geodesy Research Group, Institute of Technology Bandung,
Ganesha 10, Bandung-West Java, Indonesia
e-mail: dudy@gd.itb.ac.id

A. Tresch
Monitoring Solutions, Leica Geosystems AG,
Heinrich Wild Strasse, CH-9435 Heerbrugg, Switzerland
e-mail: ana.tresch@leica-geosystems.com

V. Nafisi
Department of Surveying Engineering, Faculty of Engineering,
University of Isfahan,
Hezar Jerib street, 81746-73441 Isfahan, Iran
e-mail: nafisi@eng.ui.ac.ir

H. Schuh
Department 1 Geodesy and Remote Sensing,
Helmholtz Centre Potsdam GFZ German Research Centre for Geosciences,
Telegrafenberg A 17, 14473 Potsdam, Germany
e-mail: schuh@gfz-potsdam.de

J. Böhm and H. Schuh (eds.), *Atmospheric Effects in Space Geodesy*,
Springer Atmospheric Sciences, DOI: 10.1007/978-3-642-36932-2_3,

Global Navigation Satellite Systems (GNSS) and Very Long Baseline Interferometry (VLBI), and those for optical techniques, like Satellite Laser Ranging (SLR), are discussed. Usually, residual tropospheric delays are estimated in the data analysis, and the parameterization needed to do so is presented. Other possibilities of correcting for the tropospheric delays are their calculation by ray-tracing through the fields of numerical weather models and by utilizing water vapor radiometer measurements. Finally, we shortly discuss how space geodetic techniques can be used in atmospheric analysis in meteorology and climatology.

1 Introduction

After the signals of the space geodetic techniques have passed through the ionosphere (see Part 2 (Alizadeh et al. 2013) for more information about the ionospheric effects) they also need to pass through the neutral atmosphere (primarly the troposphere) before they are observed at the surface of the Earth. In the troposphere the signals experience propagation delays, just as they do in the ionosphere. However, the frequency dependence of the delays is small. For microwave techniques like Global Navigation Satellite Systems (GNSS) and Very Long Baseline Interferometry (VLBI) there is practically no frequency dependence; thus it is impossible to remove the tropospheric delay with a multi-frequency combination like it is in the ionospheric case. For optical techniques like Satellite Lase Ranging (SLR) there exists a small frequency dependence and thus it is possible in principle to remove the tropospheric delays using two frequencies (see Sect. 4.3.2); however due to the amplification of the noise this is currently not practical. Thus the tropospheric delays need to be corrected for by other means.

For this part of the book it is assumed that the reader is familiar with the basic properties of the atmosphere, i.e. what is described in Part 1 (Böhm et al. 2013). We begin here with the basic description of the refractivity of the air in the neutral atmosphere (Sect. 2). Expressions for calculating the refractivity from basic meteorological measurements are presented, as well as the commonly used division of the refractivity into a hydrostatic and a wet part. In Sect. 3 these results are used for calculating the tropospheric path delay, and the properties of the hydrostatic (Sect. 3.1) and wet (Sect. 3.2) delays are discussed. The modeling of the tropospheric delays in the space geodetic data analysis is described in Sect. 4. Either the tropospheric delays are estimated in the data analysis or tropospheric delays obtained by external measurements are used. Two possible sources of external tropospheric information are considered: from ray-tracing through numerical weather models (Sect. 4.1) and inferred from microwave radiometer measurements (Sect. 4.4). The models that are commonly used when estimating the tropospheric delays in the data analysis are given in Sects. 4.2 (microwaves) and 4.3 (optical). However, since the refractivity of the atmosphere is varying randomly due to atmospheric turbulence these models are not perfect. The effects of turbulence are described in Sect. 5. This part of the book concludes with a discussion of the possible use of space geodetic techniques for studies of the atmosphere (Sect. 6).

2 Basics

The propagation of electromagnetic waves are described by Maxwell's equations (Jackson 1998). For a non-conducting, neutral medium like the troposphere these equations are

$$\nabla \cdot (\varepsilon \mathbf{E}) = 0, \tag{1}$$

$$\nabla \cdot \mathbf{B} = 0, \tag{2}$$

$$\nabla \times \mathbf{E} = -\frac{\partial \mathbf{B}}{\partial t}, \tag{3}$$

$$\nabla \times \mathbf{B} = \mu\varepsilon \frac{\partial \mathbf{E}}{\partial t}. \tag{4}$$

where $\mathbf{E}$ and $\mathbf{B}$ are the electric field and magnetic field vectors, respectively, ε the electric permittivity, μ the magnetic permeability. Assuming that the spatial and temporal variations in μ and ε are small, the equations can be combined into forming a wave equation for the electric field.

$$\nabla^2 \mathbf{E} = \mu\varepsilon \frac{\partial^2 \mathbf{E}}{\partial t^2} = \frac{n^2}{c^2} \frac{\partial^2 \mathbf{E}}{\partial t^2} \tag{5}$$

where $c = 1/\sqrt{\varepsilon_0 \mu_0}$ is the speed of light in vacuum and n is called the refractive index. A similar expression for the magnetic field can also be derived.

It is clear from Eq. (5) that in order to describe the propagation of a radio wave we need to know the refractive index n. In the neutral atmosphere of the Earth n is very close to one, thus it is more convenient to use the so called refractivity instead. The refractivity N (in "N-units", mm/km, or ppm) is related to the refractive index by

$$N = (n - 1) \cdot 10^6 \,. \tag{6}$$

In general the refractivity is a complex number. It can be divided into three parts

$$N = N_0 + N'(\nu) - i\,N''(\nu). \tag{7}$$

In case the spatial and temporal variations of N are small, i.e. the variations over one wavelength or one period are negligible, the effect on the propagation of electromagnetic waves caused by the real and the imaginary parts of the refractivity can be considered separately. For the signals of space geodetic techniques traveling through the atmosphere, this separation is a reasonable assumption since the wavelengths are shorter than a few decimeters. The real part of the refractivity ($N_0 + N'(\nu)$) causes refraction and propagation delay of signals traveling through the atmosphere. It consists of a frequency-independent (non-dispersive) part N_0 and a frequency-dependent (dispersive) part $N'(\nu)$.

The imaginary part of the refractivity, $N''(\nu)$, causes absorption and is related to the absorption coefficient α

$$\alpha(\nu) = 10^{-6} \frac{4\pi\,\nu\,N''(\nu)}{c}. \tag{8}$$

The power W of a signal received after propagating along the path S through the atmosphere will be lower than it would have been (W_0) in vacuum (i.e. no absorption)

$$W = W_0\, e^{-\int_S \alpha(s',\nu)\,\mathrm{d}s'} = W_0\, e^{-\tau(\infty,\nu)}, \tag{9}$$

where $\tau(\infty, \nu)$ is called the opacity.

Since the observables of space geodetic techniques (e.g. GNSS, VLBI, and SLR) typically are measurements of the travel time of the signals, the absorption is typically not important since it does not affect the propagation delay. Of course, absorption will affect the delay measurements by increasing the noise; higher attenuation will cause the signal-to-noise-ratio to be lower, and thus the accuracy of the measured delay will be worse (in the worst case the signal cannot be detected). However, there is typically no need for modeling this effect in the space geodetic data analysis. Thus, in the following we will concentrate on the real part of the refractive index and the effects caused by it. We will come back to the absorption in Sect. 4.4, where measurements of the absorption by microwave radiometry are used to estimate the atmospheric path delay.

The (real part of) refractivity can be expressed as a function of the densities of the different atmospheric gases and the temperature T (Debye 1929)

$$N = \sum_i \left(A_i(\nu)\rho_i + B_i(\nu)\frac{\rho_i}{T} \right), \tag{10}$$

where ρ_i is the density of the ith gas, and A_i and B_i are constants. The $B_i \frac{\rho_i}{T}$ term is caused by the permanent dipole moment of the molecules. Since water vapor is the only major atmospheric gas having a permanent dipole moment, we can ignore this term for all other gases. The relative concentrations of the dry atmospheric gases are approximately constant (except carbon dioxide, see Sect. 2.1). Thus we can assume that $\rho_i = x_i\rho_d$, where x_i is constant and ρ_d is the density of dry air. This makes it possible to express the refractivity as a function of pressure, temperature, and humidity (Essen and Froome 1951)

$$\begin{aligned} N &= \sum_i A_i(\nu) x_i\, \rho_d + A_w(\nu)\rho_w + B_w(\nu)\frac{\rho_w}{T} + A_{lw}(\nu)\rho_{lw} \\ &= k_1(\nu)\frac{p_d}{T}Z_d^{-1} + k_2(\nu)\frac{p_w}{T}Z_w^{-1} + k_3(\nu)\frac{p_w}{T^2}Z_w^{-1} + k_4(\nu)\rho_{lw}, \end{aligned} \tag{11}$$

where ρ_{lw} is the density of liquid water. It is here assumed here that the liquid water droplets are small compared to the wavelength (<1 mm for microwave techniques),

for larger droplets the expression becomes more complicated (Solheim et al. 1999). However, normally the liquid water contribution to the refractivity ($k_4(\nu)\rho_{lw}$) is neglected since it is small, especially outside of clouds. The variables Z_d and Z_w are compressibility factors for dry air and water vapor, respectively. These describe the deviation of the atmospheric constituents from an ideal gas. The compressibility factor for the ith constituent of air is given by

$$Z_i = \frac{p\,M_i}{\rho_i R T}, \tag{12}$$

where M_i is the molar mass and R is the universal gas constant. For an ideal gas we have $Z = 1$. Owens (1967) obtained expressions for Z_d^{-1} and Z_w^{-1} by a least squares fitting to thermodynamic data. These expressions are (for p_d and p_w in hPa and T in K)

$$Z_d^{-1} = 1 + p_d \left[57.97 \cdot 10^{-8} \left(1 + \frac{0.52}{T} \right) - 9.4611 \cdot 10^{-4} \frac{T - 273.15}{T^2} \right], \tag{13}$$

$$Z_w^{-1} = 1 + 1650 \frac{p_w}{T^3} \left[1 - 0.01317\,(T - 273.15) + 1.75 \cdot 10^{-4} (T - 273.15)^2 + 1.44 \cdot 10^{-6} (T - 273.15)^3 \right]. \tag{14}$$

2.1 Microwaves

Figure 1 shows the total refractivity for frequencies between 0 and 100 GHz for the case when the total pressure is 1013 hPa, the temperature is 300 K, and the relative humidity is 100 % (and for three different values for the concentration of liquid water). The refractivity was calculated using the Millimeter-wave Propagation Model (MPM) (Liebe 1985, 1989; Liebe et al. 1993). As can be seen, the variations in the refractivity as function of frequency are relatively small. The biggest variations are in the range 50–70 GHz, a region where several strong absorption lines exist for oxygen. Below 40 GHz the refractivity is more or less constant. There are small variations around the 22.235 GHz water vapor absorption line, however these can typically be neglected. Since all space geodetic techniques that use microwaves operate at frequencies well below 40 GHz, we can consider the refractivity to be frequency independent for microwaves. Thus the phase ($c_p = c_0/n$) and group velocities ($c_g = c_0/(n + f\,\partial n/\partial f)$) in the troposphere will be equal.

In Fig. 1 three different cases are shown corresponding to different concentrations of liquid water: 0 g/m^3, 0.05 g/m^3 (e.g. fog), and 1 g/m^3 (e.g. inside a cloud). The impact of liquid water on the refractivity is typically neglected since it is relatively small, although in order to achieve highest accuracy in the presence of dense clouds the effect should be considered. The difference between the case with 1 g/m^3 liquid water and the case with no liquid water is about 1.44 mm/km for the frequencies below 10 GHz, and then it decreases slightly with frequency to about 1.35 mm/km

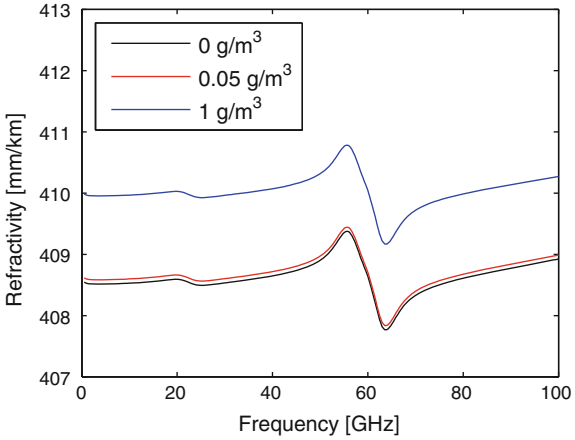

Fig. 1 The total refractivity as function of frequency. The total pressure is 1013 hPa, the temperature 300 K, and the relative humidity is 100 %. Three different cases are shown corresponding to different concentrations of liquid water: 0, 0.05, and 1 g/m^3

at 100 GHz. This agrees with the published values for k_4 in the microwave range, which is generally about 1.45 (Liebe et al. 1993; Solheim et al. 1999).

By ignoring the liquid water term and assuming that the refractivity is frequency independent, Eq. (11) becomes

$$N = k_1 \frac{p_d}{T} Z_d^{-1} + k_2 \frac{p_w}{T} Z_w^{-1} + k_3 \frac{p_w}{T^2} Z_w^{-1}. \tag{15}$$

Several different laboratory measurements have been performed in order to determine the constants k_1, k_2, and k_3 (e.g. Boudouris 1963, Bevis et al. 1994). Thayer (1974) estimated these constants by extrapolating measurements made at optical frequencies to the microwave region. The claimed accuracy was better than what is obtained from other investigations due to more accurate refractivity measurements being available for optical frequencies. However, as pointed out by e.g. Hill et al. (1982) extrapolation of optical measurements is problematic due to several resonance frequencies in the infrared region, thus the values published by Thayer (1974) should not be used. Rüeger (2002a,b) summarized and discussed many of these investigations, and calculated the "best average" values for the constants. These values are given in Table 1. The accuracy of k_1 is 0.015 % and the accuracy of the water vapor part of the refractivity is 0.15 %.

Strictly speaking the constant k_1 is dependent on the relative concentrations of the different dry atmospheric gases, thus if these change k_1 will also change. Most dry atmospheric gases have stable concentrations. Of the major gases only the concentration of carbon dioxide show a significant variation (it is increasing with 1.5–2 ppm/year). Rüeger (2002a) gives a formula for calculating k_1 for different carbon dioxide concentrations. In total the carbon dioxide makes k_1 about 0.03 % larger compared to a carbon dioxide free atmosphere. The k_1 value given by Rüeger

Table 1 The "best average" values of the k_1, k_2, and k_3 coefficients in Eq. (15), as presented by Rüeger (2002a,b)

	k_1 (K/hPa)	k_2 (K/hPa)	k_3 (K^2/hPa)
375 ppm CO_2	77.6890	71.2952	375463
392 ppm CO_2	77.6900	71.2952	375463

For k_1 two values are given corresponding to two different carbon dioxide concentrations: 375 ppm (2004 level, used by Rüeger (2002a,b) and 392 ppm (2012 level)

(2002a,b) assumed a carbon dioxide concentration of 375 ppm (2004 level). Table 1 also shows k_1 for a carbon dioxide concentration of 392 ppm (2012 level). The concentration of carbon dioxide also shows an annual variation of about 5 ppm, meaning that k_1 will have an annual variation of about $2.8 \cdot 10^{-4}$ K/hPa. This variation is negligible for all practical purposes.

Using Eq. (12) it is possible to rewrite Eq. (15) as

$$N = k_1 \frac{R}{M_d}\rho + k_2' \frac{p_w}{T} Z_w^{-1} + k_3 \frac{p_w}{T^2} Z_w^{-1} = N_h + N_w, \tag{16}$$

where $k_2' = k_2 - k_1 \frac{M_w}{M_d}$ and:

$$N_h = k_1 \frac{R}{M_d}\rho, \tag{17}$$

$$N_w = k_2' \frac{p_w}{T} Z_w^{-1} + k_3 \frac{p_w}{T^2} Z_w^{-1}. \tag{18}$$

N_h is called the hydrostatic refractivity and N_w the wet (or non-hydrostatic) refractivity. The hydrostatic refractivity depends only on the total density of air, while the wet part depends only on the partial pressure of water vapor and the temperature. Figure 2 shows examples of vertical profiles of N_h and N_w. While the hydrostatic part

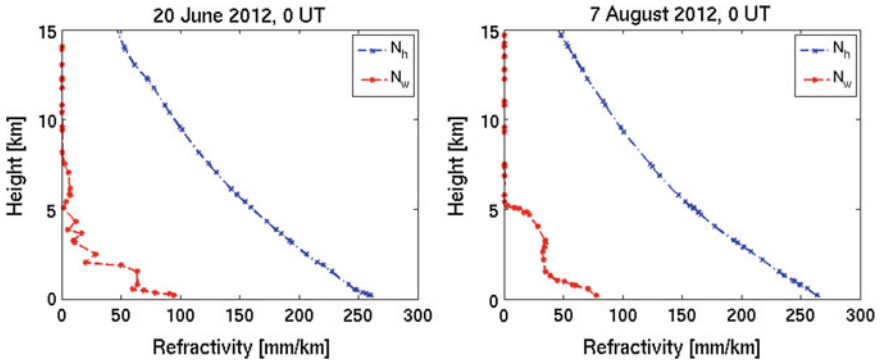

Fig. 2 Examples of vertical profiles of the hydrostatic and wet refractivity. The profiles are calulated using radiosonde data from Vienna, Austria

is larger than the wet part, the wet refractivity is much more variable and difficult to model. We will see in Sect. 3.1 that the effect of the hydrostatic refractivity on the propagation of microwaves can be accurately estimated from just the surface pressure, while the modeling of the wet part is more complicated.

It should be noted that in the literature sometimes a division of the refractivity into a dry and a wet part is used (e.g. Perler et al. 2011). The dry refractivity will be the part caused only by the first term of the righthand side of Eq. (15), while the other two terms are designated as the wet part. It is important to remember that the wet refractivity obtained in this case is not the same as the wet (i.e. non-hydrostatic) refractivity obtained when dividing the refractivity into a hydrostatic and wet part (Eq. 18). The division into dry and wet parts makes sense in that it clearly separates the contributions from the dry gases and water vapor (part of the hydrostatic refractivity is caused by water vapor). However, there are practical advantages of using the division into hydrostatic and wet parts, making it more commonly used. As shown in Sect. 3.1 the propagation delay caused by the hydrostatic refractivity can easily be inferred from surface pressure measurements.

2.2 Optical Refractivity of Moist Air

For optical frequencies, the coefficient k_3 in Eq. (11) is very small and can be ignored. However, the frequency dependence of the k_1 and k_2 coefficients needs to be considered. Normally the refractivity is expressed as a function of the density of dry air and water vapor (see Born and Wolf 1999, pp. 95–103)

$$\begin{aligned} N &= k_1(\nu)\frac{p_d}{T}Z_d^{-1} + k_2(\nu)\frac{p_w}{T}Z_w^{-1} = k_1(\nu)\frac{R}{M_d}\rho_d + k_2(\nu)\frac{R}{M_w}\rho_w \\ &= \tilde{k}_d(\nu)\rho_d + \tilde{k}_w(\nu)\rho_w. \end{aligned} \tag{19}$$

$\tilde{k}_d(\nu)$ and $\tilde{k}_w(\nu)$ are the dispersions of dry air and water vapor components, respectively. ρ_d and ρ_w are the density of dry air and water vapor, respectively.

Similarly for microwaves, N can also be divided into a hydrostatic and a non-hydrostatic (wet) part

$$N = N_h + N_w, \tag{20}$$

where

$$N_h = \tilde{k}_d(\nu)\rho_t, \tag{21}$$

$$N_w = \tilde{k}_w^{\star}(\nu)\rho_w, \tag{22}$$

$$\tilde{k}_w^{\star}(\nu) = \tilde{k}_w(\nu) - \tilde{k}_d(\nu). \tag{23}$$

In the literature, the dispersion formulae for $\tilde{k}_d(\nu)$ and $\tilde{k}_w(\nu)$ proposed by various investigators such as Edlén (1966), Barrell and Sears (Jeske 1988, p. 217),

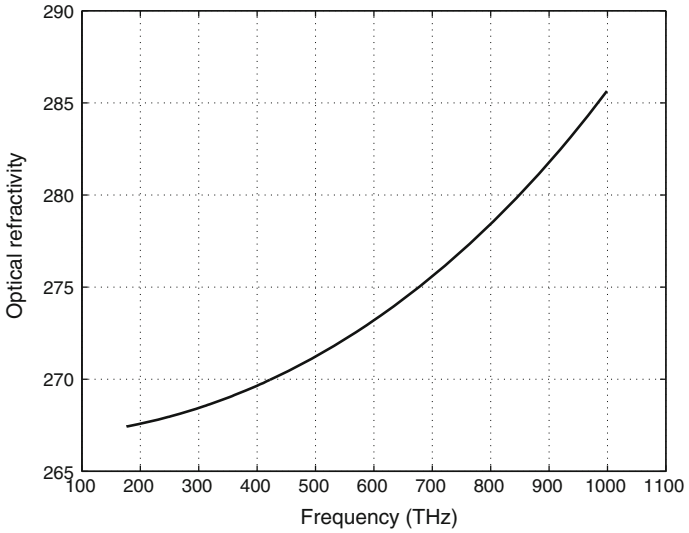

Fig. 3 The total optical refractivity as function of frequency. The total pressure is 1013 hPa, the Temperature 300 K, and the relative humidity is 100 %

Owens (1967), Ciddor (1996), and Ciddor and Hill (1999) can be used. For the accurate calculation of the optical refractivity, IAG has recommended (Rüeger 2002b, Chap. 3) the formulae proposed by Ciddor (1996) and Ciddor and Hill (1999) that are expressed as

$$\tilde{k}_d(\nu) = \frac{1}{\rho_{ds}} \left(\frac{5792105}{238.0185 - \Upsilon^2} + \frac{167917}{57.362 - \Upsilon^2} \right) (1 + 0.534 \times 10^{-6}(x_c - 450)) \times 10^{-2}, \tag{24}$$

$$\tilde{k}_w(\nu) = \frac{1.022}{\rho_{ws}} \left(295.235 + 2.6422\Upsilon^2 - 0.032380\Upsilon^4 + 0.004028\Upsilon^6 \right) \times 10^{-2}, \tag{25}$$

where ρ_{ds} is the density of dry air at 15 °C, 101325 Pa, $x_w = 0$ (where $x_w = p_w/p$ is the molar fraction of water vapor in moist air). ρ_{ws} is the density of pure water vapor at 20 °C, 1333 Pa, $x_w = 1$. Υ is the wave number (reciprocal of the wavelength, $\frac{1}{\lambda} = \frac{\nu}{c_0}$) and x_c is the fractional carbon dioxide content. A plot of the optical refractivity as function of frequency is shown in Fig. 3.

3 Definition of Path Delay in the Neutral Atmosphere

In space geodesy normally the travel time (or difference in travel time) between a source in space (a satellite or a quasar) to a receiver on the surface of the Earth is

measured. This travel time is then converted to a distance measurement by multiplying with the speed of light in vacuum. The atmosphere will introduce an error in this distance since it will affect the propagation path of the signal and since the propagation speed of the signal in the atmosphere is lower than the speed of light in vacuum.

If the variations in the refractivity over the distance of one wavelength is negligible we can use the geometric optics approximation. This means that the propagation of an electromagnetic wave can be described as a ray. When calculating the propagation time of the electromagnetic wave we thus only have to consider the refractivity along the ray path. For the propagation of the signals used in space geodesy the wavelengths are a few decimeters at most, thus in the Earth's atmosphere this approximation will normally be valid. The electric path length L (propagation time divided by the speed of light in vacuum) of a ray propagating along the path S through the atmosphere will be

$$L = \int_S n(s)\,\mathrm{d}s. \tag{26}$$

The electric path will be longer than the geometric length G of a straight line between the endpoints of the path for two reasons (see Fig. 4). Firstly, the propagation velocity is lower in the atmosphere than in vacuum. Secondly, the path S taken by the ray is, according to Fermat's principle, the path which minimizes L. The atmospheric delay, ΔL, is defined as the excess electric path length caused by the atmosphere

$$\Delta L = L - G = \int_S n(s)\mathrm{d}s - G = \int_S [n(s) - 1]\,\mathrm{d}s + \int_S ds - G = 10^{-6}\int_S N(s)\,\mathrm{d}s + S - G, \tag{27}$$

where S is the geometric length of the actual propagation path of the ray. By dividing the refractivity into hydrostatic and wet parts using Eq. (16) we get

$$\Delta L = 10^{-6}\int_S N_h(s)\,\mathrm{d}s + 10^{-6}\int_S N_w(s)\,\mathrm{d}s + S - G = \Delta L_h + \Delta L_w + S - G, \tag{28}$$

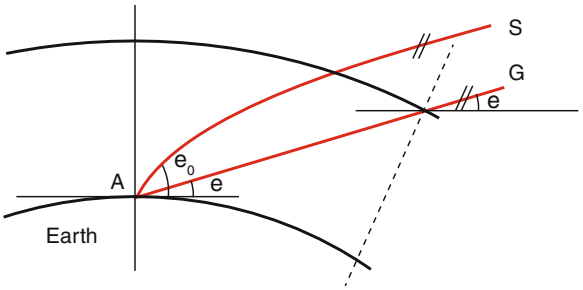

Fig. 4 Path taken by a signal through the atmosphere. The signal will take the path with the shortest propagation time (S). Since the signal propagates slower in the atmosphere than in vacuum, the geometrical length of S will be larger than the straight path G

where ΔL_h and ΔL_w are called the hydrostatic and wet delay, respectively. Commonly, the effect of bending, $S - G$, is by convention considered to be part of the hydrostatic delay, i.e. the hydrostatic mapping function (see Sect. 4.2) includes the bending effect.

In space geodesy it is common to refer the slant delays to the delays in the zenith direction (using mapping functions, see Sect. 4.2). The zenith hydrostatic delay ΔL_h^z and the zenith wet delay ΔL_w^z are given by

$$\Delta L_h^z = 10^{-6} \int_{h_0}^{\infty} N_h(z)\, \mathrm{d}z, \tag{29}$$

$$\Delta L_w^z = 10^{-6} \int_{h_0}^{\infty} N_w(z)\, \mathrm{d}z, \tag{30}$$

where h_0 is the altitude of the site.

3.1 Hydrostatic Delay

From Eqs. (17) and (29) we see that the hydrostatic delay only depends on the total density and not on the mixing ratio of wet and dry parts. Following Davis et al. (1985), the hydrostatic delay can be determined by using the hydrostatic equation

$$\frac{\mathrm{d}p}{\mathrm{d}z} = -\rho\,(z)\, g\,(z), \tag{31}$$

where $g(z)$ is the gravity along the vertical coordinate z, and integration of Eq. (31) yields the pressure p_0 at the height h_0

$$p_0 = \int_{h_0}^{\infty} \rho\,(z)\, g\,(z)\, \mathrm{d}z = g_{eff} \int_{h_0}^{\infty} \rho\,(z)\, \mathrm{d}z. \tag{32}$$

Instead of the height-dependent gravity $g(z)$, we introduce the mean effective gravity g_{eff}

$$g_{eff} = \frac{\int_{h_0}^{\infty} \rho\,(z)\, g\,(z)\, \mathrm{d}z}{\int_{h_0}^{\infty} \rho\,(z)\, \mathrm{d}z}, \tag{33}$$

and the inversion yields the height h_{eff} which is the height of the center of mass of the atmosphere above the site and can be determined with

$$h_{eff} = \frac{\int_{h_0}^{\infty} \rho\,(z)\, z \mathrm{d}z}{\int_{h_0}^{\infty} \rho\,(z)\, \mathrm{d}z}. \tag{34}$$

Saastamoinen (1972b) used the approximation for the effective height

$$h_{eff} = (0.9h_0 + 7300\,\mathrm{m}) \pm 400\,\mathrm{m}, \tag{35}$$

which holds for all latitudes and all seasons.

3.1.1 Microwaves

With the pressure p_0 at the site, it is now possible to determine the zenith hydrostatic delay

$$\Delta L_h^z = 10^{-6} k_1 \frac{R\,p_0}{M_d\,g_{eff}}. \tag{36}$$

We follow Saastamoinen (1972b) and Davis et al. (1985) to find the appropriate coefficients in Eq. (36). At first, the gravity g_{eff} at the effective height h_{eff} is determined with

$$g_{eff} = 9.8062\left(1 - 0.00265\cos(2\theta) - 0.31 \cdot 10^{-6} h_{eff}\right), \tag{37}$$

which combined with Eq. (35) can be written as

$$g_{eff} = g_m \cdot f(\theta, h_0), \tag{38}$$

with $g_m = 9.7840$ and

$$f = \left(1 - 0.00266\cos(2\theta) - 0.28 \cdot 10^{-6} h_0\right), \tag{39}$$

where θ and h_0 are latitude and orthometric (or ellipsoidal) height of the station. Thus, the zenith hydrostatic delay is

$$\Delta L_h^z = 10^{-6} k_1 \frac{R\,p_0}{M_d\,g_m f(\theta, h_0)}, \tag{40}$$

and after substitution of all values we get for the zenith hydrostatic delay in meters

$$\Delta L_h^z = 0.0022768 \frac{p_0}{f(\theta, h_0)}, \tag{41}$$

where p_0 is in hPa. The molar masses M_d and M_w stay constant up to heights of about 100 km (Davis 1986), which is essential for all troposphere delay models. The errors in the zenith hydrostatic delays are mainly caused by errors in k_1 and in the surface pressure measurements. At typical meteorological conditions the zenith hydrostatic delays are about 2.3 m at sea level. An error in the surface pressure of 1 hPa causes an error of about 2.3 mm. In order to reach an accuracy of 0.1 mm, the pressure has to be measured with an accuracy of 0.05 hPa. The error due to the assumption of hydrostatic equilibrium depends on the wind and is about 0.01 % (0.2 mm path delay). Under severe weather conditions vertical accelerations can reach 1% of the

gravity acceleration, which can cause errors in the zenith hydrostatic delays of about 20 mm (Davis et al. 1985).

3.1.2 Optical Zenith Hydrostatic Delays

The optical zenith hydrostatic delay can, just as for microwaves, be expressed as a function of the surface pressure. The derivation is in principle the same and will not be repeated here. The final expression is

$$\Delta L_h^z = 0.1022\ \tilde{k}_d(\nu) \times 10^{-6} \frac{p_0}{f(\theta, h_0)}. \tag{42}$$

The above equation is slightly different from the one developed by Mendes and Pavlis (2004), which is expressed as

$$\Delta L_h^z = 24.16579 f_h(\nu) \times 10^{-6} \frac{p_0}{f(\theta, h_0)}. \tag{43}$$

Mendes and Pavlis (2004) derived their own dispersion factor $f_h(\nu)$ based on the modified dispersion formula in Eq. (24) for the wavelength of 0.532 μm. Equations (42) and (43) produce similar accuracy results if they are applied to real SLR observations.

3.1.3 Pressure Values

For the analysis of space geodetic techniques, there are three possibilities to obtain pressure values at the stations: local pressure recordings at the sites, pressure values from numerical weather models, or empirical models for the pressure (Böhm et al. 2009a). For instance, simple empirical models are the ones by Berg (1948)

$$p = 1013.25 \cdot (1 - 0.0000226h)^{5.225}, \tag{44}$$

with the pressure p in hPa and orthometric station height h in m, or the model by Hopfield (1969)

$$p = 1013.25 \cdot \left(\frac{T_k - \alpha h}{T_k}\right)^{\frac{g}{R_d \alpha}}, \tag{45}$$

with the atmospheric temperature at sea level $T_k = 293.16$ K, the normal lapse rate of temperature with elevation $\alpha = 4.5$ K/km, gravity g at the surface of the Earth (9.7867 m/s^2) and the gas constant $R_d = 0.287$ kJ/K/kg for dry air. More sophisticated empirical models are UNB3m (Leandro et al. 2006) or Global Pressure and Temperature (GPT; Böhm et al. (2007)). UNB3m is based on meteorological parameters (pressure, temperature, humidity, temperature lapse rate, and water vapor pressure

Table 2 Availability of pressure values from local recordings at the sites, from numerical weather models (e.g. the hydrostatic zenith delays from ECMWF data as provided by the Vienna University of Technology), and from the empirical model GPT

Pressure	Local recordings	Grid values	GPT
Availability	At sites	All (by interpolation)	All
Time span	Per observation	Since 1994	Unlimited
Spatial resolution	Per site	2.0 x 2.5°	Spherical harmonics (9/9)
Time resolution	Per observation	6 h	Annual

height factor) at five latitude bands which are symmetric w.r.t. the equator (similar to the Niell Mapping Functions (Niell 1996)). Input parameters for GPT are station latitude, longitude, height and the day of the year, which is similar to the Global Mapping Functions (GMF; Böhm et al. 2006a) as both, GPT and GMF, are based on spherical harmonics up to degree and order 9.

Table 2 summarizes some properties of the pressure values (or zenith hydrostatic delays) from different sources. Unfortunately, local pressure measurements are usually not available, in particular at GNSS stations. Thus, to get consistent values of a priori zenith hydrostatic delays for global GNSS networks it is preferable to take these values from numerical weather models. For example, the Department of Geodesy and Geoinformation (GEO) at the Vienna University of Technology provides zenith hydrostatic delays calculated from ECMWF data. These are provided on global grids (2.5° times 2.0°) and with a temporal resolution of 6 h starting in 1994 (Böhm et al. 2009a). For scientific purposes also forecast values are made available so that they can be used for real-time applications without significant loss of accuracy (Böhm et al. 2009b). Empirical models like GPT are always available for all time epochs, but the spatial resolution is limited as it is represented by spherical harmonics up to degree and order 9 (≈20° in latitude/longitude), respectively. The model only includes an annual variation with the zero phase set to 28 January, so it cannot capture short-term and sub-annual weather phenomena. As an example, Fig. 5 shows pressure values at station O'Higgins in Antarctica. It is evident that empirical models like the model by Berg (1948) or GPT cannot describe the short term pressure variations and that the model by Berg (1948) is offset by about 20 hPa.

We have also compared and validated the empirical models Berg and GPT with pressure values from the ECMWF on global grids (10° in latitude times 12.5° in longitude) (Böhm et al. 2009a). The comparison was performed for the year 2005 and the temporal resolution was 10 days (i.e. one global grid was taken every 10 days and consequently 36 grids were used for the statistics). An error in the pressure of 1 hPa corresponds (at sea level) to approximately a 2.3 mm error in the L_h^z. This error will result in an error in the position—especially the vertical component – estimated with a space geodetic technique. In Sect. 4.2 a rule of thumb relating the error in the delay to the error in the vertical coordinate is presented, from this we find that 3 hPa (7 mm zenith delay error) correspond to 1 mm station height difference. It was found that the Berg model has large deficiencies especially around Antarctica, resulting in

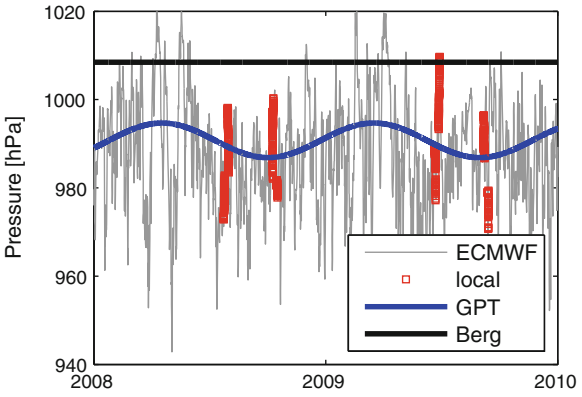

Fig. 5 Pressure values for station O'Higgins in Antarctica from the ECMWF (*grey line*), local pressure recordings at the radio telescope (*red squares*), GPT (*blue line*), and pressure determined with the model by Berg (1948) (*black bold line*)

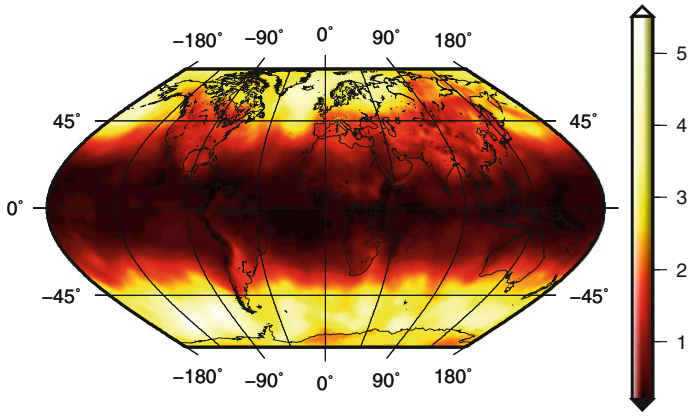

Fig. 6 Simulated station height standard deviations in mm for GPT with respect to the pressure values provided by the ECMWF (based on 36 epochs in 2005 for a 2° latitude times 2.5° longitude grid) (modified from Böhm et al. (2009b))

station height errors of more than 10 mm. The errors for GPT for this region are smaller, and these might completely disappear with an increased degree and order of the spherical harmonic expansion. There are almost no biases for the rest of the Earth (see Böhm et al. (2009b)).

GPT only accounts for an annual variation of the pressure with rather small amplitudes compared to the other (e.g. weekly) variations of the pressure. Thus, the standard deviations of the differences to the grid values from the ECMWF are almost the same for the Berg model (constant pressure per site) and GPT. In Fig. 6 the simulated station height standard deviations are plotted for the case of using GPT compared pressure values from the ECMWF. There is an increase of the standard deviations

towards higher latitudes (with maximum values at around ±60° latitude), which is due to the larger pressure variations in these regions compared to equatorial regions (Böhm et al. 2009a).

3.2 Wet Delay

3.2.1 Microwave Zenith Wet Delays

From Eq. (30) the zenith wet delay is

$$\Delta L_w^z = 10^{-6}\left[\int_{h_0}^{\infty}\left(k_2'\frac{p_w}{T}Z_w^{-1}\right)\mathrm{d}z + \int_{h_0}^{\infty}\left(k_3\frac{p_w}{T^2}Z_w^{-1}\right)\mathrm{d}z\right]. \tag{46}$$

The first term in Eq. (46) is about 1.6 % of the second term.

The derivation of a model to account for the zenith wet delay (ΔL_w^z) is by far more challenging than the one for the hydrostatic delay. This is due to high spatial and temporal variability and unpredictability of the amount of water vapor. Thus, the temperature and the water vapor content at the Earth surface are not representative for the air masses above. This is the reason why numerous models have been developed over the past few decades for the wet delay, while preserving Saastamoinen's model (with slight modifications) for determining the hydrostatic delay. The zenith wet delay varies between a few mm at the poles and about 40 cm above the equatorial regions. In order to keep millimeter accuracy in space geodetic techniques, the ΔL_w^z is nowadays estimated as an additional parameter within the data analysis. Nevertheless, some models are listed below and can be used as an initial value in the data analysis or for applications not requiring high accuracy.

Saastamoinen (1972b) proposes the calculation of the zenith wet delay ΔL_w^z based on ideal gas laws using a simple relation

$$\Delta L_w^z = 0.0022768(1255 + 0.05T_0)\frac{p_{w0}}{T_0}, \tag{47}$$

where p_{w0} is the water vapor pressure and T_0 is the temperature at the surface. Similar to the hydrostatic delay, Hopfield (1969) proposes an expression for ΔL_w^z as follows

$$\Delta L_w^z = \frac{10^{-6}}{5}N_w(h_0)h_w, \tag{48}$$

with $N_w(h_0)$ the refractivity of wet air at the surface (located at height h_0) and a mean value $h_w = 11000$ m for the height of the troposphere up to which water vapor exists. Ifadis (1986) proposes to model the zenith wet delay as a function of surface pressure, partial water vapor pressure and temperature. Mendes and Langley (1998) derived a linear relation between ΔL_w^z and partial water vapor pressure. Some other

models are being described by Mendes (1999). An approximate relation between water vapor pressure and delay reads

$$\Delta L_w^z \approx \frac{0.217 p_w}{T}. \tag{49}$$

Assuming an isothermal atmosphere with exponential decrease of water vapor pressure p_w, and assuming that water vapor exists until a height of 2 km, we get an approximation for the wet delay as a function of water vapor pressure at the Earth's surface p_{w0}

$$\Delta L_w^z \approx 748 \frac{p_{w0}}{T_0^2}. \tag{50}$$

An even simpler way is a rule of thumb that suggests that the wet zenith delay in cm equals the water vapor pressure in hPa at the Earth's surface

$$\Delta L_w^z \,[\text{cm}] \approx p_{w0}\,[\text{hPa}]. \tag{51}$$

In any case, information of water vapor pressure and/or temperature at the surface has to be known. If no surface meteorological observation is available, we can use the simple model of the standard atmosphere where p_w can be calculated as a function of the relative humidity f, i.e.

$$p_w = \frac{f}{100} \exp(-37.2465 + 0.213166T - 0.000256908T^2). \tag{52}$$

3.2.2 Conversion of Zenith Wet Delays to Precipitable Water

The zenith wet delay can be related to the amount of integrated water vapor above the station. Following Eq. (46) and using the expression for integrated mean temperature T_m (Bevis et al. 1992)

$$T_m = \frac{\int_s (\frac{e}{T} Z_w^{-1}) \mathrm{d}s}{\int_s (\frac{e}{T^2} Z_w^{-1}) \mathrm{d}s} \approx \frac{\int_{h_0}^{\infty} (\frac{e}{T} Z_w^{-1}) \mathrm{d}z}{\int_{h_0}^{\infty} (\frac{e}{T^2} Z_w^{-1}) \mathrm{d}z}, \tag{53}$$

we can write

$$\Delta L_w = 10^{-6} \left[k_2' + \frac{k_3}{T_m} \right] \int_s \left(\frac{e}{T} Z_w^{-1} \right) \mathrm{d}s. \tag{54}$$

Applying the ideal gas laws, Eq. (54) can be reformulated as

$$\Delta L_w = 10^{-6} \left[k_2' + \frac{k_3}{T_m} \right] \frac{R}{M_w} \int_s \rho_w \mathrm{d}s. \tag{55}$$

To be able to calculate the mean temperature T_m the vertical profiles of the water vapor and temperature have to be known. Such data can be obtained from radiosonde measurements or calculated (and predicted) from operational meteorological models (Wang et al. 2005). In absence of this data, the empirically derived model by e.g. Bevis et al. (1992) and Emardson and Derks (2000) can be used. The determination of the mean temperature T_m from Eq. (53) is based on the weighting with water vapor pressure in the atmosphere. Since water vapor is mainly located near the Earth surface the mean temperature T_m will be highly correlated with the temperature at the Earth surface T_0. Using 8718 profiles of radiosonde launches at 13 stations in the United States between 27 and 65° northern latitude, between 0 and 1600 m height, and over a time span of 2 years Bevis et al. (1992) found

$$T_m \approx 70.2 + 0.72 T_0, \tag{56}$$

with a standard deviation of ± 4.74 K. If ΔL_w^z and surface temperature are known without error, the integrated water vapor can be computed with an average error of less than 4 %.

It is clear from Eq. (55) that the wet delay is proportional to the integrated water vapor content IWV ($IWV = \int_0^\infty \rho_w \, dz$). Since IWV is a variable that can be easily obtained from numerical weather prediction models or measured by other techniques, it is of great interest to have a simple expression for calculating the wet delay from IWV, and vice versa. Thus we define the proportionality constant Π such that

$$IWV = \Pi \, \Delta L_w^z, \tag{57}$$

where ΔL_w^z is the wet tropospheric delay in the zenith direction. By comparing Eqs. (55) and (57), we find that Π can be related to T_m by

$$\Pi = \frac{10^6 M_w}{\left[k_2' + \frac{k_3}{T_m}\right] R}, \tag{58}$$

The integrated water vapor in zenith direction can also be provided as precipitable water (PW) which corresponds to the height of the equivalent water column above the station

$$PW = \frac{IWV}{\rho_{w,fl}}, \tag{59}$$

where $\rho_{w,fl}$ is the density of liquid water in kg/m^3. With a dimensionless quantity κ we can relate the ΔL_w^z and PW

$$PW = \kappa \Delta L_w^z, \tag{60}$$

with κ defined as

$$\kappa = \frac{\Pi}{\rho_{w,fl}}. \tag{61}$$

The precipitable water is roughly 0.16 of ΔL_w^z. This value can vary by more than 15 %, mainly as a function of latitude and season (Fölsche 1999).

Errors in the factor Π are mainly caused by errors in T_m and the constants in Eq. (58). According to Fölsche (1999) the influence of errors in the mean temperature is at least one order of magnitude larger than errors in the constants. It is shown in the following how accurate T_m has to be determined to get the amount of water vapor with a certain accuracy.

The partial derivative of Π with respect to the mean temperature yields

$$\frac{\partial \Pi}{\partial T_m} = \frac{10^6 M_w k_3}{R\left[k_2' + \frac{k_3}{T_m}\right]^2 T_m^2}. \tag{62}$$

This means that Π is changed by about 20 kg/m^3 if $T_m (= 270$ K) is changed by 4 K. Assuming a zenith wet delay of 200 mm this corresponds to an error in the precipitable water of about 4 mm. Requirements for better accuracies of PW (1 mm or better) indicate that the real weather data should be used to derive the mean temperature instead of approximations such as provided in Eq. (56).

3.2.3 Optical Zenith Wet Delays

Substituting Eq. (22) into Eq. (30) yields

$$\Delta L_w^z = 10^{-6} \tilde{k}_w^\star(\nu) \int_{h_0}^{\infty} \rho_w(z)\, \mathrm{d}z. \tag{63}$$

Following Saastamoinen (1972a), the integral $\int_{h_0}^{\infty} \rho_w(h)\, \mathrm{d}h$ can be approximated by

$$\int_{h_0}^{\infty} \rho_w(z)\, \mathrm{d}z \approx \frac{R_d}{4 g_m} p_{w0}, \tag{64}$$

where p_{w0} is the surface pressure of water vapor. Substituting Eq. (64) into Eq. (30), the zenith wet delay of optical measurements can be modeled as

$$\Delta L_{w0}^z = 10^{-6} \tilde{k}_w^\star(\nu) \frac{R_d}{4 g_m} p_{w0}. \tag{65}$$

Equation (65) is slightly different from the one developed by Mendes and Pavlis (2004), which is expressed as

$$\Delta L^z_{w0} = 10^{-6}(5.316 f_{nh}(\nu) - 3.759 f_h(\nu)) \frac{R_d}{4 g_m} p_{w0}. \quad (66)$$

Mendes and Pavlis (2004) derived their own dispersion factors $f_h(\lambda)$ and $f_{nh}(\lambda)$ based on the modified dispersion formula in Eq. (24) for the 0.532 μm wavelength. Equations (65) and (66) produce similar accuracy results if they are applied to real SLR observations.

4 Modeling Delays in the Neutral Atmosphere

There are basically two ways to handle the atmospheric delays when analyzing space geodetic data; either external measurements of the atmospheric delays are used to correct the measurements, or the atmospheric delays are parameterized and estimated in the data analysis. As seen in Sect. 3.1 the hydrostatic delay can be accurately determined from surface pressure measurements. However, the wet delay cannot be estimated that accurately from meteorological measurements at the surface. Thus it is common when analyzing space geodetic data to use surface pressure measurements to model the hydrostatic delay, while the wet delay is estimated in the data analysis. In the data analysis the tropospheric delays are modeled using mapping functions and gradients (see Sect. 4.2). An alternative strategy is to also use external estimates of the hydrostatic and wet delays. Such estimates could for example be obtained from ray-tracing though numerical weather models (Sect. 4.1), a technique also commonly applied for deriving expression for the tropospheric mapping functions. Another possibility is to infer the tropospheric delay from measurements by external instruments such as Water Vapor Radiometers (WVR) (Sect. 4.4). The numerical values etc. given in these sections are for microwaves, although the general principles could of course also be applied in the case of optical techniques. Tropospheric modeling for optical frequencies (e.g. SLR) is discussed in Sect. 4.3.

4.1 Ray-Tracing

From e.g. radiosonde data or numerical weather prediction models we can calculate the refractivity field of the atmosphere. This could be used to estimate the atmospheric delay simply by integrating the refractivity along the propagation path of the signal. However, the problem is that we normally do not exactly know the propagation path. To discover it we can apply the so-called ray-tracing technique. The ray-tracing technique has been used in many fields of science where the propagation of an electro-magnetic wave through a stratified medium has to be quantified. The ray-tracing is based on the so-called Eikonal equation, which represents the solution of

the Helmholtz equation for an electro-magnetic wave propagating through a slowly varying medium (Iizuka 2008; Wheelon 2001). Using the Eikonal equation, we can determine the ray path and the optical path length. In the following sub-sections, we present a ray-tracing system that can be applied for tropospheric modeling and discuss some basic elements in tropospheric ray-tracing calculations through Numerical Weather Prediction Models.

4.1.1 Eikonal Equation and Ray Path

To derive the Eikonal equation we start from Maxwell's equations (Eqs. 1–4). It is convenient to use the H-field $\mathbf{H}$ instead of the magnetic field $\mathbf{B}$, where $\mathbf{H}$ is defined by

$$\mathbf{B} = \mu \mathbf{H}. \tag{67}$$

We can consider a general time-harmonic field

$$\mathbf{E}(r,t) = \mathbf{e}(\mathbf{r}) e^{i(k_0 L(\mathbf{r}) - 2\pi\nu t)}, \tag{68}$$

$$\mathbf{H}(r,t) = \mathbf{h}(\mathbf{r}) e^{i(k_0 L(\mathbf{r}) - 2\pi\nu t)}, \tag{69}$$

where $L(\mathbf{r})$ is the optical path, and $\mathbf{e}(\mathbf{r})$ and $\mathbf{h}(\mathbf{r})$ are (complex) vector functions. The wave number for vacuum (k_0) is defined as

$$k_0 = \frac{2\pi\nu}{c} = \frac{2\pi}{\lambda_0}, \tag{70}$$

where λ_0 is the vacuum wavelength. By inserting these equations into Maxwell's equations (Eqs. 1–4) and assume that there are no free charges and zero conductivity, we get after some calculations (Born and Wolf 1999)

$$\nabla L \times \mathbf{h} + c\,\varepsilon \mathbf{e} = -\frac{1}{ik_0} \nabla \times \mathbf{h}, \tag{71}$$

$$\nabla L \times \mathbf{e} - c\,\mu \mathbf{h} = -\frac{1}{ik_0} \nabla \times \mathbf{e}, \tag{72}$$

$$\mathbf{e} \cdot \nabla L = -\frac{1}{ik_0} \left(\mathbf{e} \cdot \frac{\nabla \varepsilon}{\varepsilon} + \nabla \cdot \mathbf{e} \right), \tag{73}$$

$$\mathbf{h} \cdot \nabla L = -\frac{1}{ik_0} \left(\mathbf{h} \cdot \frac{\nabla \mu}{\mu} + \nabla \cdot \mathbf{h} \right). \tag{74}$$

For small vacuum wavelength, and therefore large wave number for vacuum (k_0)

$$\nabla L \times \mathbf{h} + c\,\varepsilon \mathbf{e} = \mathbf{0}, \tag{75}$$

$$\nabla L \times \mathbf{e} - c\,\mu \mathbf{h} = \mathbf{0}, \tag{76}$$

$$\mathbf{e} \cdot \nabla L = 0, \tag{77}$$

$$\mathbf{h} \cdot \nabla L = 0. \tag{78}$$

By eliminating **h** between Eqs. (75) and (76), and considering Eq. (77), the following differential equation is obtained which is independent of the amplitude vectors **e** and **h**

$$\|\nabla L\|^2 = n\,(\mathbf{r})^2\,, \tag{79}$$

where ∇L comprises the components of the ray directions, L is the optical path length, $n = c\sqrt{\varepsilon\mu}$ is the refractivity index of a medium, and **r** is the position vector. This equation is the well-known Eikonal equation. The surfaces $L(\mathbf{r}) = constant$ are called geometrical wave surfaces or the geometrical wave-fronts.

4.1.2 Hamiltonian Formalism of Eikonal Equation

The above mentioned Eikonal equation is a partial differential equation of the first order for $n\,(\mathbf{r})$ and it is possible to express it in many alternative forms. In general, the Eikonal equation can be written in the Hamiltonian canonical formalism as follows (Born and Wolf 1999; Cerveny 2005; Nafisi et al. 2012a)

$$\mathscr{H}\,(\mathbf{r}, \nabla L) = \frac{1}{\alpha}\left((\nabla L \cdot \nabla L)^{\frac{\alpha}{2}} - n(\mathbf{r})^{\alpha}\right) = 0, \tag{80}$$

$$\frac{\mathrm{d}\mathbf{r}}{\mathrm{d}u} = \frac{\partial \mathscr{H}}{\partial \nabla L}, \tag{81}$$

$$\frac{\mathrm{d}\nabla L}{\mathrm{d}u} = -\frac{\partial \mathscr{H}}{\partial \mathbf{r}}, \tag{82}$$

$$\frac{\mathrm{d}L}{\mathrm{d}u} = \nabla L \cdot \frac{\partial \mathscr{H}}{\partial \nabla L}. \tag{83}$$

Here α is a scalar value related to the parameter of interest u (see Table 3). In general it is a real number but in our applications we can consider it to be an integer. $\mathscr{H}\,(\mathbf{r}, \nabla L)$ is called Hamiltonian function or just the Hamiltonian. In a 3D space this system consists of seven equations. Six equations are obtained from Eqs. (81) and (82) must be solved together. The result of these six equations is $\mathbf{r} = \mathbf{r}(u)$ which is the trajectory of the signal in space. The seventh equation, i.e. Eq. (83), can be solved independently and yields the optical path length.

4.1.3 Ray-Tracing System for Tropospheric Modeling

Equations (80)–(82) can be used for constructing a ray-tracing system for any specific application by simply selecting a correct value for the scalar α (Nafisi et al. 2012a).

Table 3 Different cases for Hamiltonian formalism

α		Parameter of interest
0	$du = dT$	Travel time T along the ray
1	$du = ds$	Arc-length s along the ray
2	$du = d\sigma = \frac{dT}{n^2}$	Natural variables along the ray

For $\alpha = 0$, the parameter u represents travel time t along the ray. If $\alpha = 1$, the parameter u represents the arc-length s along the ray. In case of $\alpha = 2$, the parameter u is equal to dt/dn, which represents the natural variables along the ray (Cerveny 2005).

When applying ray-tracing for the determination of total delays along the ray path the natural choice is $\alpha = 1$. However, it is also possible to use $\alpha = 2$ to construct a tropospheric ray-tracing system (see Gegout et al. (2011)). Ray-tracing systems can be expressed and solved in any curvilinear coordinate system, including spherical coordinates. Selecting $\alpha = 1$ and representing the function $\mathscr{H}$ in a spherical polar coordinate system (r, θ, λ), Eq. (80) can be rewritten as

$$\mathscr{H}(r, \theta, \lambda, L_r, L_\lambda, L_\theta) \equiv \left(L_r^2 + \frac{1}{r^2} L_\theta^2 + \frac{1}{r^2 \sin^2 \theta} L_\lambda^2 \right)^{\frac{1}{2}} - n(r, \theta, \lambda) = 0, \quad (84)$$

where r is the radial distance, θ is the co-latitude, and λ is the longitude ($0 \leq \theta \leq \pi$, $0 \leq \lambda \leq 2\pi$). $L_r = \frac{\partial L}{\partial r}$, $L_\theta = \frac{\partial L}{\partial \theta}$ and $L_\lambda = \frac{\partial L}{\partial \lambda}$ are the elements of ray directions. Now, by substituting Eq. (84) into Eqs. (81) and (82), we obtain

$$\frac{dr}{ds} = \frac{1}{\beta} L_r, \quad (85)$$

$$\frac{d\theta}{ds} = \frac{1}{\beta} \frac{L_\theta}{r^2}, \quad (86)$$

$$\frac{d\lambda}{ds} = \frac{1}{\beta} \frac{L_\lambda}{r^2 \sin^2 \theta}, \quad (87)$$

$$\frac{dL_r}{ds} = \frac{\partial n(r, \theta, \lambda)}{\partial r} + \frac{1}{\beta r} \left(\frac{L_\theta^2}{r^2} + \frac{L_\lambda^2}{r^2 \sin^2 \theta} \right), \quad (88)$$

$$\frac{dL_\theta}{ds} = \frac{\partial n(r, \theta, \lambda)}{\partial \theta} + \frac{1}{\beta} \frac{L_\lambda^2}{r^2 \sin^3 \theta}, \quad (89)$$

$$\frac{dL_\lambda}{ds} = \frac{\partial n(r, \theta, \lambda)}{\partial \lambda}, \quad (90)$$

where

$$\beta = \left(L_r^2 + \frac{1}{r^2} L_\theta^2 + \frac{L_\lambda^2}{r^2 \sin^2 \theta} \right)^{\frac{1}{2}} = n(r, \theta, \lambda). \quad (91)$$

This system of equations is a direct result of Eqs. (81) and (82) in a 3D medium, and we need to solve all six differential equations simultaneously. The final output is the positions of the points along the trajectory of the ray. For solving the above ray-tracing system, the following initial conditions at the starting point (station) can be used (Nafisi et al. 2012a)

$$r = r_0, \tag{92}$$
$$\lambda = \lambda_0, \tag{93}$$
$$\theta = \theta_0, \tag{94}$$
$$L_{r0} = n_0 \cos z_0, \tag{95}$$
$$L_{\theta 0} = n_0 r_0 \sin z_0 \cos a_0, \tag{96}$$
$$L_{\lambda 0} = n_0 r_0 \sin z_0 \sin a_0 \sin \theta_0, \tag{97}$$

where a_0 and z_0 are the initial geodetic azimuth and zenith angle, respectively. In the 3D case, gradients are important factors which can affect the bending of the ray path and therefore of the total ray-traced delay. The gradient can be rewritten as

$$\nabla n(r, \lambda, \theta) = \left[\frac{\partial n(r, \theta, \lambda)}{\partial r}, \frac{1}{r} \frac{\partial n(r, \theta, \lambda)}{\partial \theta}, \frac{1}{r \sin \theta} \frac{\partial n(r, \theta, \lambda)}{\partial \lambda} \right]^T. \tag{98}$$

From a practical point of view, we must find a sophisticated technique for computing the gradients of the refractive index in Eqs. (88), (89) and (90), which are

$$\nabla n_r = \frac{\partial n(r, \theta, \lambda)}{\partial r}, \tag{99}$$
$$\nabla n_\theta = \frac{\partial n(r, \theta, \lambda)}{\partial \theta}, \tag{100}$$
$$\nabla n_\lambda = \frac{\partial n(r, \theta, \lambda)}{\partial \lambda}. \tag{101}$$

Taking the effects of the gradients on the ray-traced delay into account is important for a ray-tracing algorithm. In particular in the case of symmetries, ray-tracing in curvilinear coordinates system would be easier. However, in general the ray-tracing systems in a curvilinear coordinates are more complex and sometimes fail. A typical example in atmospheric ray-tracing is the solution for ray-tracing in spherical polar coordinates when $\theta \approx 0°$ or $\theta \approx 180°$. According to Cerveny (2005) a general solution for removing such singularities is the use of transformations between ray-tracing systems in various forms. Using standard transformation relations, a ray-tracing system represented in curvilinear coordinates can be transformed into the universal Cartesian coordinates, and after ray-tracing computations in this coordinate system the results can be again transformed back to the curvilinear coordinates. In another method suggested by Alkhalifah and Fomel (2001) a small constant parameter (δ) is added in the denominator of fractions in the ray-tracing equations to

provide numerical stability. The value of this constant must be chosen carefully; otherwise we may get unreasonable results. Other stability solutions have been suggested by Schneider (1993) and Fowler (1994). In addition, the variation of the size of the grid cells in polar coordinates can causes a stability problems, especially in presence of small-scale inhomogeneities (Fowler 1994).

By substituting Eq. (84) into Eq. (83) and solving the equation, we can obtain this well-known equation to calculate the optical path length L

$$L = \int_S n(r, \theta, \lambda) \mathrm{d}s. \tag{102}$$

Once the position of a point along the ray path has been determined by Eqs. (85)–(90), the refractivity index n and the optical path length L can be calculated using Eq. (102). As mentioned before, the total delay is defined as the difference between the optical path length L and the straight line distance G

$$\Delta L = L - G. \tag{103}$$

3D ray-tracing can be easily reduced to 2D ray-tracing by substituting $\frac{\partial n}{\partial \theta} = 0$ and $\frac{\partial n}{\partial \lambda} = 0$ into Eqs. (85)–(90). In this case, we assume that the ray does not leave a plane of constant azimuth angle. For the 2D system, the coupled partial derivatives in Eqs. (85)–(90) reduce to four equations

$$\frac{\mathrm{d}r}{\mathrm{d}s} = \frac{1}{\beta} L_r, \tag{104}$$

$$\frac{\mathrm{d}\theta}{\mathrm{d}s} = \frac{1}{\beta} \frac{L_\theta}{r^2}, \tag{105}$$

$$\frac{\mathrm{d}L_r}{\mathrm{d}s} = \frac{\partial n(r, \theta, \lambda)}{\partial r} + \frac{1}{\beta r} \left(\frac{L_\theta^2}{r^2} + \frac{L_\lambda^2}{r^2 \sin^2 \theta} \right), \tag{106}$$

$$\frac{\mathrm{d}L_\theta}{\mathrm{d}s} = \frac{1}{\beta} \frac{L_\lambda^2}{r^2 \sin^3 \theta}. \tag{107}$$

Equation (91) remains valid also for 2D ray-tracing systems. For a horizontally stratified atmosphere, further simplifications can be applied to improve the calculation speed (Thayer 1967). According to Böhm (2004), we can develop a 1D ray-tracing. Figure 7 shows the geometry of this method for a troposphere with k different refractivity layers. The geocentric distances can be estimated by adding the radius of the Earth (R_e) to the heights of each layer

$$r_i = R_e + h_i. \tag{108}$$

In this method, the elevation angles (e_i) are with respect to a horizontal plane of the station, whereas θ_i show the angles between the ray path and the tangents to the

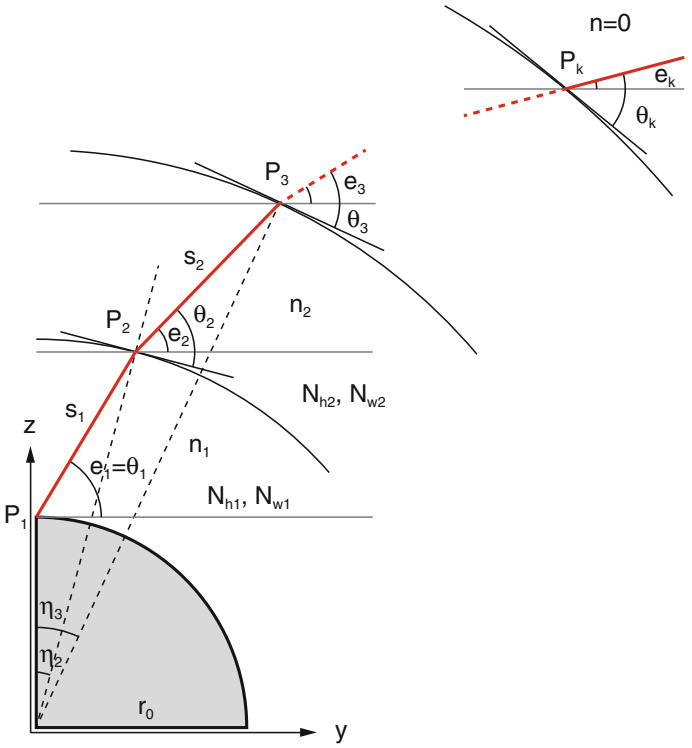

Fig. 7 Geometry of a 1D ray-tracing method, for a receiver located at P_1 and the upper limit of the troposphere at P_k. Points P_2 and P_3 show two sample points of the ray path. The y- and z-axis of the Cartesian coordinate system are parallel to horizon and zenith direction at the site, respectively. $S_2 = \|\mathbf{P}_3 - \mathbf{P}_2\|$ is the distance between two successive points along the path

layers in each intersection point of the trajectory. At the first point (receiver) these two are same, i.e. $e_1 = \theta_1$.

In this coordinate system, the z and y components are equal to r_1 and zero, respectively. Following the geometrical relation in Fig. 7 we find

$$S_i = \sqrt{r_{i+1}^2 - r_i^2 \cos\theta_i} - r_i \sin\theta_i, \tag{109}$$

$$z_{i+1} = z_i + S_i \sin e_i, \tag{110}$$

$$y_{i+1} = y_i + S_i \cos e_i, \tag{111}$$

$$\eta_{i+1} = \arctan\frac{y_{i+1}}{z_{i+1}}, \tag{112}$$

$$\delta_{i+1} = \eta_{i+1} - \eta_i, \tag{113}$$

$$\theta_{i+1} = \arccos\left(\frac{1+\eta_i \times 10^{-6}}{1+\eta_{i+1} \times 10^{-6}} \cos(\theta_i + \delta_{i+1})\right), \tag{114}$$

$$e_{i+1} = \theta_{i+1} - \eta_{i+1}. \tag{115}$$

These parameters must be calculated for all layers, and then it is possible to find the total slant delay (ΔL_d) as follow

$$\Delta L_d = \sum_{i=1}^{n-1} S_i N_i. \tag{116}$$

This equation can be divided into two terms for finding hydrostatic and non-hydrostatic components of the delay separately. By inserting h_i (along the zenith direction) instead of S_i (along the slant path) an equation for total zenith delay will be derived. As mentioned before, the bending effect is a part of the total delay and must be estimated separately. This parameter is zero for the zenith direction and

$$\Delta L_b = \sum_{i=1}^{n-1} (S_i - \cos(e_i - e_k) S_i). \tag{117}$$

for a slant direction. Implementation of the above ray-tracing system can vary substantially, with different degrees of complexity and accuracy. Examples of ray-tracing algorithms in atmospheric studies are given by Bean and Thayer (1959), Thayer (1967), Budden (1985), Davis (1986), Mendes (1999), Pany (2002), Böhm and Schuh (2003), Thessin (2005), Hulley (2007), Hobiger et al. (2008), Nievinski (2009), Wijaya (2010), Gegout et al. (2011) and Nafisi et al. (2012a). Several ray-tracing algorithms were compared by Nafisi et al. (2012b). Also it is possible to express the Eikonal equation and the ray-tracing system in curvilinear non-orthogonal coordinates systems. For details see Cerveny et al. (1988).

4.2 Mapping Functions and Gradients

In the analysis of space geodetic data the troposphere path delay $\Delta L(e)$ at the elevation angle e is usually represented as the product of the zenith delay ΔL^z and an elevation-dependent mapping function $mf(e)$ with

$$\Delta L(e) = \Delta L^z \cdot mf(e). \tag{118}$$

This concept is not only used to determine a priori slant delays for the observations, but the mapping function is also the partial derivative to estimate residual zenith delays. Typically, the zenith delay is estimated with a temporal resolution of 20–60 min in VLBI and GPS analysis. In VLBI analysis—when there is only one observation at a time at a station—this allows the zenith delays to be estimated in a least-squares adjustment. In the analysis of space geodetic observations not only the zenith delays are estimated, but also other parameters like the station clocks and the stations heights (Fig. 8). The partial derivatives of the observed delays w.r.t. the

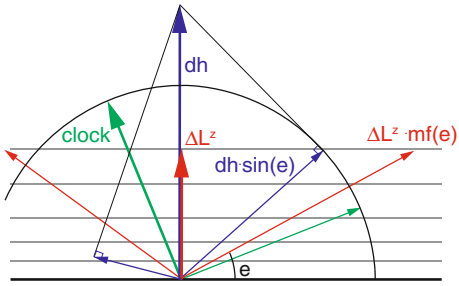

Fig. 8 Different elevation-dependence of the tropospheric delays (*red*), clock values (*green*), and height components (*blue*). Whereas the partial derivatives for the estimation of clocks and height components are strictly 1 and $\sin(e)$, respectively, the partial derivative for the estimation of the zenith delay is the mapping function which is approximately $1/\sin(e)$, but is not perfectly known (modified from Rothacher et al. (1998))

station heights are dependent on the elevation angle only, but whereas the partial derivatives w.r.t. the clocks (= 1) and the station heights (=$\sin(e)$) are exactly known, the partial derivatives for the zenith delays (i.e. the mapping functions) are only known with a limited accuracy. Consequently—via the correlations between zenith delays, station heights, and clocks—any imperfection of the mapping function will also result in errors in the station height estimates (and clock errors).

Considering Eq. (118) we find the following relationship: If the mapping function is in error (too large), then the estimated zenith delay ΔL^z is too small, because the observed tropospheric delay $\Delta L(e)$ does not change. Consequently, the estimated station height goes up. Niell et al. (2001) set up a rule of thumb specifying that the error in the station height is approximately one third of the delay error at a cutoff elevation angle of 7°. Böhm (2004) revisited this rule of thumb for VLBI analysis (and a cutoff elevation angle of 5°) specifying that the station height error is about one fifth of the delay error at the lowest elevation angle. This is close to the value 0.22 found by MacMillan and Ma (1994). The corresponding decrease of the zenith delay is about one half of the station height increase.

4.2.1 Azimuthal Symmetry: Mapping Functions

Assuming azimuthal symmetry of the neutral atmosphere around the station (i.e. at a constant elevation angle the delay is not dependent on the azimuth angle of the observation), the approach as described in Eq. (119) is used (e.g. Davis et al. 1985)

$$\Delta L(e) = \Delta L_h^z \cdot mf_h(e) + \Delta L_w^z \cdot mf_w(e). \tag{119}$$

$\Delta L(e)$ is the total path delay of the microwaves in the neutral atmosphere and e is the elevation angle of the observation to the satellite or the quasar (vacuum or geometric elevation angle). ΔL_h^z and ΔL_w^z are the a priori zenith hydrostatic and the

estimated wet delays, and $mf_h(e)$ and $mf_w(e)$ are the so-called mapping functions which provide the ratio of the delay to the delay in zenith direction. The input to both mapping functions is the vacuum elevation angle e, because the bending effect is accounted for by the hydrostatic mapping function.

Errors in the zenith hydrostatic delays or the mapping functions have an influence on station height errors as described with the rules of thumb by Niell et al. (2001) or Böhm (2004) mentioned above. The following two examples illustrate this rule of thumb, which—holding for both GPS and VLBI—depends on the actual distribution of elevation angels and on whether elevation angle-dependent weighting is used: The zenith hydrostatic and wet delays shall be 2000 and 200 mm, respectively, the minimum elevation angle is 5°, and the corresponding values for the true hydrostatic and wet mapping functions are 10.15 ($mf_h(5°)$) and 10.75 ($mf_w(5°)$) (Böhm et al. 2006b).

- We assume an error in the total pressure at the station of +10 hPa, e.g. when using the "mean" pressure from GPT during a time of low pressure. +10 hPa correspond to ≈+20 mm zenith hydrostatic delay (Saastamoinen 1972b), which is then mapped down to 5° elevation angle using the wrong mapping function (wet instead of hydrostatic, factor −0.6 = 10.15–10.75). At 5° elevation angle the mapping function error is −12 mm, and one fifth of it, i.e. −2.4 mm, would be the resulting station height error. This results in a kind of atmosphere loading correction (see Part 4, Wijaya et al. (2013)), because during a pressure low the station heights go up (Tregoning and Herring 2006; Steigenberger et al. 2009).
- We consider an error in the wet mapping function of 0.1 ($mf_w(5°) = 10.85$ instead of 10.75) or in the hydrostatic mapping function of 0.01 ($mf_h(5°) = 10.16$ instead of 10.15). The error at 5° elevation angle is in both cases 20 mm, i.e. the resulting error in the station height would be approximately +4 mm.

The scale height of the wet part in the troposphere is about 2 km, whereas the scale height of the hydrostatic part is about 8 km (cf. Fig. 9). The mapping functions describe the ratio $(AB)/(B_0B)$ (wet) and $(AC)/(C_0C)$ (hydrostatic). Due to the curvature of the Earth and the smaller scale height of the wet part, the hydrostatic

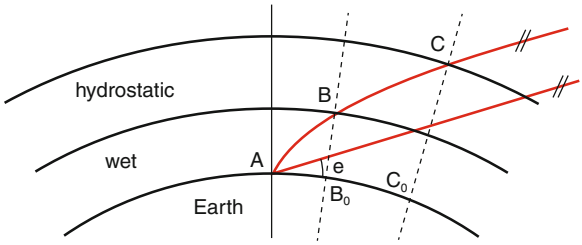

Fig. 9 The scale height of the wet part of the troposphere is about 2 km, the scale height of the hydrostatic part is about 8 km. The mapping functions describe the ratio of the paths $(AB)/(B_0B)$ (wet) and $(AC)/(C_0C)$ (hydrostatic). The wet mapping function is larger than the hydrostatic mapping function

mapping function is smaller than the wet mapping function. Exceptions are mapping functions for observations at very low elevation angles where the geometric bending effect, which is attributed to the hydrostatic mapping function, is increasing considerably. Thus, the mapping functions are a measure for the thickness of the atmosphere compared to the Earth radius (Niell et al. 2001). If the thickness of the atmosphere gets smaller, it appears to be flatter, and the mapping function approaches $1/\sin(e)$. Assuming a flat and evenly stratified atmosphere the mapping function is $1/\sin(e)$. For higher elevation angles (>20° elevation) these mapping functions are sufficiently accurate. Marini (1972) showed that the dependence on the elevation angle of the mapping functions for any horizontally stratified atmosphere can be described with continued fractions, when a, b, c, etc. are constants (Eq. 120). For verification Marini (1972) used standard atmosphere data but no real weather data.

$$mf(e) = \cfrac{1}{\sin(e) + \cfrac{a}{\sin(e) + \cfrac{b}{\sin(e) + \cfrac{c}{\sin(e) + \ldots}}}}. \tag{120}$$

This concept was first used in a model for the refraction of the hydrostatic atmosphere (Marini and Murray 1973) which has since then been applied in the analysis of geodetic and astrometric VLBI observations for a long time. The zenith delay corresponds to that by Saastamoinen (1972b), and the mapping functions are represented by a continued fraction form with two coefficients a and b. The first mapping functions for space geodetic applications with different coefficients for the hydrostatic and wet parts were published by Chao (1974) who replaced the second $\sin(e)$ by $\tan(e)$ to get unity in zenith direction.

Davis et al. (1985) developed the mapping function CfA2.2 for the hydrostatic delays down to 5° elevation; it is based on the approach by Chao (1974) but extended by an additional constant c. Based on ray-tracing through various standard atmospheres with elevation angles between 5 and 90°, the coefficients a, b, and c were determined as functions of pressure, water vapor pressure, and temperature at the Earth surface, and from vertical temperature gradients and the height of the troposphere. Herring (1992) developed coefficients for the mapping function MTT (MIT Temperature) as functions of latitude, height, and the temperature at the site. Unlike Davis et al. (1985) he did not use standard atmospheres but radiosonde data. The MTT mapping functions are based on a slightly changed continued fraction form which is widely accepted nowadays

$$mf(e) = \cfrac{1 + \cfrac{a}{1 + \cfrac{b}{1 + c}}}{\sin(e) + \cfrac{a}{\sin(e) + \cfrac{b}{\sin(e) + c}}}. \tag{121}$$

The factor in the denominator ensures that the mapping function is equal to one in the zenith direction. The strong dependence of the MTT mapping function (Herring 1992) on surface temperature induced Niell (1996) to develop the New Mapping Functions (NMF, now often called Niell Mapping Functions). The NMF do not use meteorological parameters at the sites, but only the day of the year (doy), station latitude, and station height as input parameters. Thus, they can be easily applied at stations without meteorological sensors, which often is the case for GNSS stations. Niell (1996) used standard atmosphere data at various latitudes to determine hydrostatic and wet mapping functions down to 3° elevation. Similar to Davis et al. (1985) and Herring (1992), he used ray-tracing methods to determine the coefficients a, b, and c of the continued fraction form in Eq. (121). NMF is based on sine functions to describe the temporal variation of the coefficients. The period is 365.25 days and the maximum/minimum is set to January 28 (doy 28). There is also a height correction for the hydrostatic NMF (NMFh) which describes that mapping functions increase with increasing height, i.e. the atmosphere above the site becomes flatter.

Niell (2000) was the first to determine mapping functions from numerical weather models which are often available with a time resolution of 6 h. For the Isobaric Mapping Functions (IMF), he used empirical functions for b and c, and he determined the coefficients a of the continued fraction in Eq. (121) from re-analysis data of the Goddard Space Flight Center Data Assimilation Office (DAO) (Schubert et al. 1993). For the hydrostatic IMF he used the height of the 200 hPa pressure level which is readily available with most numerical weather models and which is describing the thickness of the atmosphere well. For the wet IMF Niell suggested to use a coarse ray-trace at 3.3° initial elevation angle through numerical weather models. However, some practical and conceptual limitations in the computation of the wet IMF induced Böhm and Schuh (2004) to develop the Vienna Mapping Functions (VMF).

Thus, the VMF are characterized by the removal of some weaknesses of the IMFw, e.g. the coarse vertical resolution of weather model data is improved by vertical interpolation and the bending effect is taken into account rigorously. The same approach is applied for the wet and the hydrostatic mapping function, i.e. a ray-tracing is performed at an initial elevation angle of 3.3° for the hydrostatic and wet components yielding the hydrostatic delay, the wet delay, as well as the bending effect and the outgoing (vacuum) elevation angle which is ≈3°. (Please notice that always the refractivity profile above the site vertical is used, which makes the 1D ray-tracing simple and causes the delays to be symmetric with azimuth.) Together with the zenith hydrostatic and wet delays which are also determined by ray-tracing, the hydrostatic and wet mapping functions (Eq. (121)) at the outgoing elevation angle are calculated. The geometric bending effect is added to the hydrostatic mapping function. Similar to IMF, empirical functions are used for the b and c coefficients, which allows the determination of a in Eq. (121) by simple inversion. Since the coefficients a, b, and c are highly correlated, small errors in b and c can easily be compensated with the a coefficients. However, Böhm et al. (2006b) improved the b and c coefficients, and consequently the a coefficients had to be re-calculated. The coefficients of the so-called VMF1 are $b_h = 0.0029$, $b_w = 0.00146$, $c_w = 0.04391$, and the coefficient c_h is provided with Eq. (122) and Table 4

Table 4 Parameters c_0, c_{10}, c_{11}, and ψ needed for computing the coefficient c of the hydrostatic mapping function

Hemisphere	c_0	c_{10}	c_{11}	ψ
Northern	0.062	0.001	0.005	0
Southern	0.062	0.002	0.007	π

Mind that the c_{xx} coefficient is incorrect in the paper by Böhm et al. (2006b)

Table 5 Parameters c_0, c_{10}, c_{11}, and ψ needed for computing the coefficient c of the total mapping function

Hemisphere	c_0	c_{10}	c_{11}	ψ
Northern	0.063	0.000	0.004	0
Southern	0.063	0.001	0.006	π

$$c_h = c_0 + \left(\left(\cos\left(\frac{\text{doy} - 28}{365.25} \cdot 2\pi + \psi\right) + 1\right) \cdot \frac{c_{11}}{2} + c_{10}\right) \cdot (1 - \cos\theta). \quad (122)$$

The VMF1 are valid (tuned) for elevation angles above 3°, and the largest deviations from ray-traces at other elevations show up at about 5° elevation angle. The Vienna Mapping Function 1 is realized as discrete time series (resolution 6 h) of coefficients a, either on a global grid or at certain geodetic sites (see http://ggosatm.hg.tuwien.ac.at/). Mind that with the gridded version of the VMF1, the height correction of Niell (1996) has to be applied.

Instead of separating the delays into a hydrostatic and a wet part, an alternative concept of total mapping functions has also been investigated for troposphere delay modeling (Böhm et al. 2006b), i.e. the use of a single total mapping function mf_t (Eq. 123) both for mapping down the a priori zenith total delays $\Delta L^z_{t,0}$ and as partial derivative for the estimation of the residual total delays $\Delta L^z_{t,res}$ (Eqs. 124 and 125). Table 5 summarizes the parameters for the c_t coefficient which have been determined with the same approach as the c_h coefficients of the hydrotstatic VMF1. The b coefficient of the total VMF1 is also $b_t = 0.0029$.

$$mf_t(e) = \frac{\Delta L_h(e) + \Delta L_w(e) + \Delta L_{bend}}{\Delta L^z_h + \Delta L^z_w}, \quad (123)$$

$$\Delta L^z_t = \Delta L^z_h + \Delta L^z_w = \Delta L^z_{t,0} + \Delta L^z_{t,res}, \quad (124)$$

$$\Delta L(e) = \Delta L^z_{t,0} \cdot mf_t(e) + \Delta L^z_{t,res} \cdot mf_t(e). \quad (125)$$

Although a priori zenith total delays are required in the data analysis, a priori zenith hydrostatic delays can also be applied because the mapping function for the a priori zenith delays is the same as for the residual zenith delays (this only holds if there are no constraints on the estimated zenith delays). With the classical separation into a hydrostatic and a wet part, errors of the a priori zenith hydrostatic delays cannot be fully compensated by the estimation of the remaining wet part since the hydrostatic and wet mapping functions are not identical, especially at low elevation angles. The advantage of the concept of total mapping functions is that the results are not affected

by poor a priori zenith hydrostatic delays (Böhm et al. 2006b). On the other hand, the value of total mapping function is close to that of the hydrostatic mapping function, so it cannot account for the rapid variation of the wet zenith delays which occurs even between the 6 hourly epochs of the total VMF1. Thus, it is preferable to keep the separation into a hydrostatic and a wet mapping function, at least as long as the time resolution is not 3 h or better.

The goal of the Global Mapping Functions (GMF; Böhm et al. 2006a) is to make available mapping functions which can be used globally and implemented easily in existing geodetic data analysis softwares and which are consistent with NWM-based mapping functions, in particular with the VMF1 (Böhm et al. 2006b). Compared to the NMF (Niell 1996), the parameterization of the coefficients in the three-term continued fraction (Eq. 121) has been refined to include also a longitude dependence. Using global grids of monthly mean profiles for pressure, temperature, and humidity from the ECMWF 40 years reanalysis data (ERA40), the coefficients a_h and a_w were determined using data from the period September 1999 to August 2002 applying the same strategy and the same b and c coefficients used for VMF1. Thus, at each of the 312 grid points, 36 monthly a values were obtained for the hydrostatic and wet mapping functions, respectively. The hydrostatic coefficients were reduced to mean sea level by applying the height correction given by Niell (1996). The mean values, a_0, and the annual amplitudes, A, of the sinusoidal function (Eq. 126) were fitted to the a parameter time series of each grid point, with the phases referred to January 28, corresponding to the NMF. The standard deviations of the monthly values at the single grid points with respect to the values obtained from Eq. (126) increase from the equator towards larger latitudes, with a maximum value of 8 mm (expressed as equivalent station height error) in Siberia. For the wet component, the standard deviations are generally smaller, with the maximum values being about 3 mm at the equator Böhm et al. (2006a).

$$a = a_0 + A \cdot \cos\left(\frac{\text{doy} - 28}{365.25} \cdot 2\pi\right), \tag{126}$$

$$a_0 = \sum_{n=0}^{9} \sum_{m=0}^{n} P_{nm}(\sin\theta)(A_{nm}\cos(m\lambda) + B_{nm}\sin(m\lambda)). \tag{127}$$

Then, the global grid of the mean values a_0 and that of the amplitudes A for both the hydrostatic and wet coefficients of the continued fraction form were expanded into spatial spherical harmonic coefficients up to degree and order 9 (according to Eq. (127) for a_0) in a least-squares adjustment. The residuals of the global grid of a_0 and A values to the spherical harmonics are in the sub-millimeter range (in terms of station height). The hydrostatic and wet coefficients a for any site coordinates and day of year can then be determined using Eq. (126).

In Fig. 10 VMF1 and GMF hydrostatic mapping functions at 5° elevation angle are plotted for Fortaleza, Brazil. The GMF reflects a seasonal variability and, in this respect, agrees well with the VMF1. However, a deficiency is evident in the empirical mapping function compared to the VMF1 because GMF does not reveal

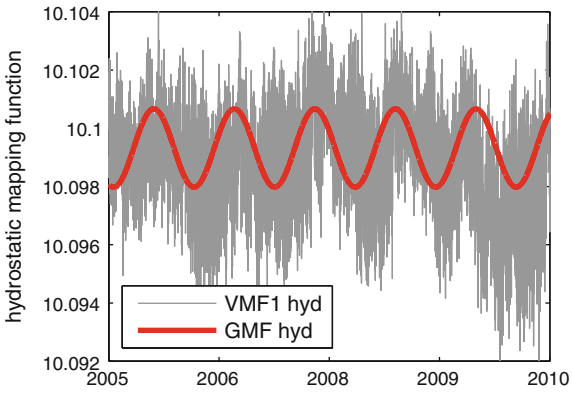

Fig. 10 Hydrostatic mapping functions VMF1 and GMF at 5° elevation at Fortaleza, Brazil. Phenomena such as the El Niño event in 2009 cannot be captured with empirical mapping functions like GMF that contain only average seasonal terms

the special meteorological conditions described by the VMF1 during the El Niño event in 2009/10.

Niell (2006) compared the mapping functions VMF1, IMF, GMF, and NMF with mapping functions derived from ray-tracing of radiosonde data in 1992, which were assumed to be the most accurate reference possible. The standard deviation was converted to station height scatter with the rule of thumb by Niell et al. (2001) (one third of the delay at 7° elevation angle). The best agreement was found for the VMF1, both for the hydrostatic and the wet mapping function. All hydrostatic mapping functions show the lowest scatter at the equator, because there are only small pressure and temperature variations. The scatter increases with station latitude, in particular for the empirical GMF and NMF, which of course cannot account for the variations at synoptic time scales (∼10 days). The situation is different for the wet mapping functions where the scatter is largest at the equator. This is due to the fact that the zenith wet delays are largest over the equator (up to 40 cm). At the poles, there is hardly any humidity; thus, errors in the wet mapping functions are not critical for the estimation of station heights (and zenith wet delays). Again, the performance of the wet VMF1 is best. However, it has to be mentioned here that the radiosonde data might have been assimilated in the NWM which are used to determine the VMF1 and IMF. Consequently the station height scatter for these two mapping functions may be too optimistic.

There have been many investigations comparing the application of different mapping functions in VLBI or GPS analysis. For example, Böhm et al. (2007) and Steigenberger et al. (2009) compared various mapping functions in GPS analysis, and Tesmer et al. (2007) compared them in VLBI analysis. Moreover, Kouba (2008) compared the gridded VMF1 against the VMF1 determined for specific sites, or Böhm et al. (2009b) assessed the accuracy of forecast VMF1 for the application in real time analysis.

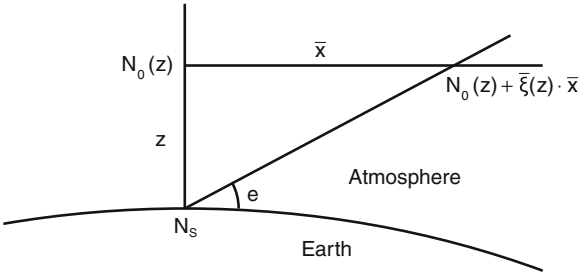

Fig. 11 The refractivity in the vicinity of the vertical profile above the site can be determined with the linear horizontal gradients of refractivity ξ

4.2.2 Azimuthal Asymmetry: Gradients

Mapping functions as described above allow for the modeling of path delays under the assumption of azimuthal symmetry of the neutral atmosphere around the station. Consequently, vertical refractivity profiles above the sites are sufficient to determine the path delays at arbitrary elevation angles or the mapping functions, respectively, because the refractivity is always taken from the vertical profile as it is the case for the VMF1. However, due to certain climatic and weather phenomena path delays will not be constant at varying azimuths. For example, at sites at northern latitudes the path delay towards south will be systematically larger than towards north, because the height of the troposphere above the equator is larger than above the poles.

In the following the derivation of linear horizontal gradients is shown following Davis et al. (1993). The Taylor series up to degree one for the refractivity at a station is (Fig. 11)

$$N(\mathbf{x}, z) = N_0(z) + \boldsymbol{\xi}(z) \cdot \mathbf{x}, \tag{128}$$

$$\xi_i(z) = \left. \frac{\partial N(\mathbf{x}, z)}{\partial x_i} \right|_{\mathbf{x}=0}. \tag{129}$$

$N_0(z)$ is the refractivity above the site, $\mathbf{x}$ is the horizontal position vector (origin is placed at the site), and $\boldsymbol{\xi}(z)$ is the linear horizontal gradient vector of refractivity at height z. The index i refers to the i-th component of $\mathbf{x}$: 1 towards north and 2 towards east. The path delay (hydrostatic or wet) at an arbitrary direction can be found by integration of Eq. (128) along the path s. If expressed with elevation angle e and azimuth angle a, we get

$$\Delta L(a, e) = 10^{-6} \int_0^\infty N(s)\, \mathrm{d}s = 10^{-6} \int_0^\infty N_0(z)\, \mathrm{d}s + 10^{-6} \int_0^\infty \boldsymbol{\xi}(z) \cdot \mathbf{x}\, \mathrm{d}s, \tag{130}$$

$$\Delta L(a, e) = \Delta L_0(e) + 10^{-6} \int_0^\infty \boldsymbol{\xi}(z) \cdot \mathbf{x}\, \mathrm{d}s, \tag{131}$$

where ΔL_0 is the delay without gradients. In Eq. (131) the difference between the paths with and without gradients has been neglected. Davis et al. (1993) state that this difference is as large as 1 mm for $N = 300$, $\partial N/\partial x_i = 1\ \mathrm{km}^{-1}$, and $e = 20°$. If the concept of an azimuth-dependent mapping function is used, Eq. (131) can be written as

$$\Delta L(a, e) = \Delta L^z \cdot mf(a, e), \tag{132}$$

with

$$mf(a, e) = mf_0(e) + \delta mf(a, e) = mf_0(e) + 10^{-6} \int_0^\infty \boldsymbol{\zeta}(z) \cdot \mathbf{x}\, \mathrm{d}s, \tag{133}$$

where

$$\boldsymbol{\zeta}(z) = \frac{\boldsymbol{\xi}(z)}{\Delta L^z}, \tag{134}$$

and mf_0 and ΔL^z are the mapping function and the path delay in zenith direction for the symmetric case. Thus, the gradients cause a change in the mapping function which can be described by an additional term δmf. With

$$\mathbf{x}(a, e) \approx z \cdot \cot(e')(\cos(a)\hat{\mathbf{n}} + \sin(a)\hat{\mathbf{e}}), \tag{135}$$

$$ds \approx \mathrm{d}z \cdot mf_0(e), \tag{136}$$

and normalized gradients of refractivity

$$\boldsymbol{\zeta}(z) = \zeta_n \cdot \hat{\mathbf{n}} + \zeta_e \cdot \hat{\mathbf{e}}, \tag{137}$$

and when $\hat{\mathbf{n}}$ and $\hat{\mathbf{e}}$ refer to the unit vectors in north and east direction and e' is the refracted elevation angle (which only differs from the geometric elevation angle at low elevations), we get

$$\delta mf(a, e) \approx 10^{-6} mf_0(e)\ \cot(e') \left(\cos(a) \int_0^\infty z \cdot \zeta_n(z) \cdot \mathrm{d}z + \sin(a) \int_0^\infty z \cdot \zeta_e(z) \cdot \mathrm{d}z \right), \tag{138}$$

and

$$\delta mf(a, e) = mf_0(e) \cot(e')(Z_n \cos(a) + Z_e \sin(a)), \tag{139}$$

when

$$\mathbf{Z} = 10^{-6} \int_0^\infty z \cdot \boldsymbol{\zeta}(z)\, \mathrm{d}z. \tag{140}$$

Equation (138) shows that the elevation-dependence of the azimuth-dependent mapping function $\delta mf(a, e)$ consists of two parts: the dependence on mf_0 and on the factor $\cot(e')$. As already mentioned the mapping functions are dependent on the geometric elevation angle e, whereas the cotangent depends on the refracted eleva-

tion angle e', because close to the site this angle determines the refraction. It holds that

$$e' = e + \delta e(e), \tag{141}$$

where δe can be described with (Davis et al. 1993)

$$\delta e \approx 10^{-6} N_S \cot(e). \tag{142}$$

N_S is the refractivity at the Earth surface, and for $N_S = 300$, $e = 5°$ we get $\delta e \approx 0.2°$. Since δe is small, $\cot(e')$ can be expanded into a series, and we get for the deviation from the symmetric mapping function

$$\delta mf(a, e) = mf_0(e) \cot(e)(1 - 10^{-6} N_S \csc^2(e))(Z_n \cos(a) + Z_e \sin(a)). \tag{143}$$

With the delay gradients (or just gradients) $\mathbf{G}$

$$\mathbf{G} = \mathbf{Z} \cdot \Delta L^z, \tag{144}$$

we get for the path delay

$$\Delta L(a, e) = \Delta L_0(e) + mf_0(e) \cot(e)(1 - 10^{-6} N_S \csc^2(e))(G_n \cos(a) + G_e \sin(a)). \tag{145}$$

The equations above can be used to determine gradients by integrating over the horizontal gradients of refractivity along the site vertical (see e.g. MacMillan and Ma (1997), Böhm and Schuh (2007))

$$G_a = 10^{-6} \int_0^\infty \xi_a \, z \, \mathrm{d}z, \tag{146}$$

where a denotes the azimuth direction (e.g. e or n). Figure 12 shows refractivity gradients at the site vertical for the station Fortaleza.

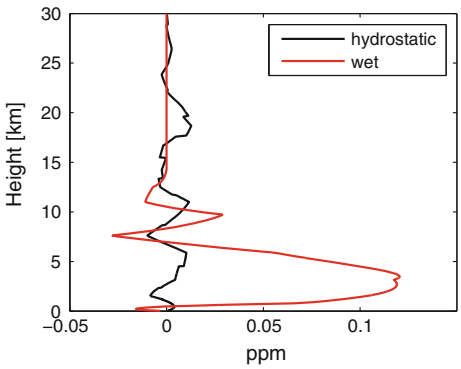

Fig. 12 Weighted (with height) refractivity gradients ($dN(z) \cdot z$) towards east at Fortaleza (Brazil) on 21 November 2011 at 0:00 UT. The *black line* shows the hydrostatic, the *red line* the wet gradients

In the following it is shown how gradients can be interpreted. Equation (128) can be written in the form

$$N(\mathbf{x}, z) = N_0(z)(1 + \boldsymbol{\alpha} \cdot \mathbf{x}), \tag{147}$$

$$\boldsymbol{\alpha} = \boldsymbol{\xi}(z)/N_0(z), \tag{148}$$

with the constant vector $\boldsymbol{\alpha}$. This means that the relative gradient of refractivity is constant, and we get for the gradient of the delay

$$\mathbf{G} = 10^{-6}\,\boldsymbol{\alpha} \int_0^\infty z\, N_0(z)\, \mathrm{d}z. \tag{149}$$

Supposing that refractivity decreases exponentially with height, i.e.

$$N_0(z) = N_S\, e^{-z/H}, \tag{150}$$

and H is the scale height, we get for the integral in Eq. (149) the expression

$$\mathbf{G} = 10^{-6}\boldsymbol{\alpha} \cdot N_S \cdot H^2, \tag{151}$$

and for the gradient of refractivity

$$\boldsymbol{\xi}(z) = 10^6 \frac{\mathbf{G}}{H^2} e^{-z/H}. \tag{152}$$

The scale height H is the height of the neutral atmosphere (or of a part of it) if the density is constant with height and the total mass is conserved. For the gradients of refractivity at the Earth surface we get

$$\boldsymbol{\xi}(z) = 10^6 \frac{\mathbf{G}}{H^2}. \tag{153}$$

This shows that for a given value of $\mathbf{G}$ the gradients of refractivity $\boldsymbol{\xi}$ are inversely proportional to the squared scale heights H. A typical value for the gradients $\mathbf{G}$ is 1 mm. This corresponds to a path delay of ≈65 mm at 7° elevation. Assuming a scale height H of 1 km the gradient of refractivity $\boldsymbol{\xi}$ is $1\,\mathrm{km}^{-1}$. With a scale height of 8 km $|\boldsymbol{\xi}| = 0.015\ \mathrm{km}^{-1}$. Hydrostatic atmospheric gradients which are caused by pressure and temperature gradients, have a large spatial resolution of about 100 km (Gardner 1976) and a temporal resolution of hours to days. Wet gradients have a small spatial resolution (<10 km) and they can vary at hourly time scales or faster, although longer time scales are also possible (e.g. at coastal regions). Wet gradients are functions of water vapor pressure and temperature.

Presently, two models for the gradients are used in the analysis of space geodetic techniques. These are the model by MacMillan (1995) that follows Davis et al. (1993) and the model by Chen and Herring (1997). Both concepts will be described below.

Furthermore, it is shown that the concept of horizontal gradients corresponds to a tilting of the mapping functions. This is used by Niell (2001) who uses the tilting of the 200 hPa pressure level to get hydrostatic gradients. MacMillan (1995) proposes to use the simple model

$$\Delta L(a, e) = \Delta L_0(e) + mf_h(e)\cot(e)(G_n \cos(a) + G_e \sin(a)), \tag{154}$$

i.e. the difference between e and e' is neglected. Chen and Herring (1997) use the gradient model

$$\Delta L(a, e) = \Delta L_0(e) + mf_g(e)(G_n \cos(a) + G_e \sin(a)), \tag{155}$$

$$mf_g(e) = \frac{1}{\sin(e)\tan(e) + C}, \tag{156}$$

and

$$C = \frac{3\int \xi \cdot z^2 \cdot \mathrm{d}z}{2\int \xi \cdot z \cdot (z + R_e) \cdot \mathrm{d}z}. \tag{157}$$

After integration they get for the coefficient C

$$C = 3H/R_e. \tag{158}$$

For scale heights of 6.5 km for the hydrostatic part and 1.5 km for the wet part of the neutral atmosphere, they find the values 0.0031 and 0.0007 for the hydrostatic and wet coefficients C, respectively. For the estimation of total gradients, Herring (1992) suggests using 0.0032.

Gradients can also be interpreted by a tilting of the mapping function (Rothacher et al. 1998) see Fig. 13. The basic relations are shown below assuming that the atmosphere is flat (mapping function $1/\sin(e)$) and that the path delay in zenith direction is not changed by the tilting. If the gradient G is the deflection of the path

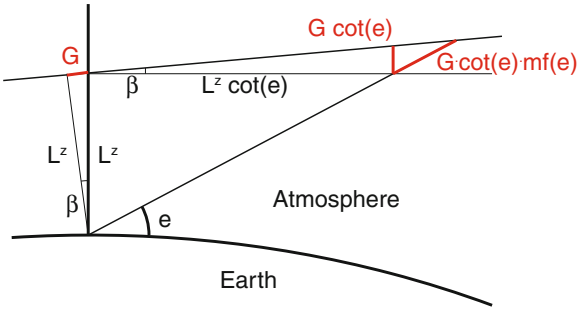

Fig. 13 Tilting of the mapping function by the angle β assuming a horizontally stratified atmosphere

delay in zenith direction due to the tilting angle β, it is shown that the path delay at the elevation angle e due to the gradients is $\cot(e)mf(e)G$, which is exactly what is proposed by MacMillan (1995). Starting with

$$\Delta L(e-\beta) = \Delta L^z \cdot mf(e-\beta) \approx \Delta L^z \left(mf(e) + \frac{\partial mf}{\partial e}(-\beta) \right), \tag{159}$$

and using $1/\sin(e)$ as mapping function and with

$$\beta = G/L^z, \tag{160}$$

we get

$$\Delta L(e-\beta) = \Delta L^z \cdot mf(e) + \cot(e)mf(e)G. \tag{161}$$

A gradient G of 1 mm corresponds to tilting angles of 1.5' (hydrostatic) and 17' (wet). The effects on the zenith delays are $2 \cdot 10^{-4}$ and $2 \cdot 10^{-5}$ mm, respectively, and can be neglected.

It is important to estimate gradients in the analysis of space geodetic observations, in particular when observing at low elevation angles. On the other hand, there is no need to apply a priori gradients if no constraints are applied on the estimation of gradients.

4.3 Atmospheric Delays for SLR

4.3.1 Single-Color SLR Observations

The accuracy of the results obtained from Satellite Laser Ranging (SLR) measurements is ultimately limited by the atmospheric propagation effects (as well as by by the hardware system). In the 1970s, Marini and Murray (1973) developed a model to correct the atmospheric delays in SLR measurements and their model became a standard correction model at that time. In the early 2000s, Mendes et al. (2002) pointed out some limitation in that model, namely as regards the modeling of the elevation dependency of the zenith atmospheric delays (the mapping function component of the model). Thus, Mendes et al. (2002) developed their mapping functions (FCULa and FCULb) that represents significant improvement over the mapping functions of the Marini-Murray model. Of particular interest is the ability of the new mapping functions to be used in combination with any zenith delay model, i.e. Mendes and Pavlis (2004) model, used to predict the atmosphere delay in the zenith direction.

Similar to the microwave frequencies, the mapping functions are normally modeled using Eq. (121). New mapping functions have been developed based on ray-tracing through one full year (1999) of radiosonde data from 180 stations, globally distributed, with a variable number of balloon launches per day. Two different parameterizations were proposed by Mendes et al. (2002) with the coefficients in Eq. (121)

written as functions of the selected parameters. One parameterization of the mapping function (FCULa) requires both site location and meteorological (surface temperature) data. The coefficients of the mapping function have the following mathematical formulation

$$a = a_0 + a_1\ T_0 + a_2\ \cos\theta + a_3\ h_0, \tag{162}$$

where T_0 is the temperature at the station in degrees centigrade, θ is the station latitude, and h_0 is the orthometric height of the station, in meters. The coefficients b and c are modeled similarly.

The second parameterization (FCULb) does not depend on any meteorological data, i.e. similar to the model developed by Niell (1996) for radio wavelengths. For this function, the coefficients have the following form

$$a = a_0 + (a_1 + a_2\ \theta_d^2)\cos\left(\frac{2\pi}{365.25}\ (\text{doy} - 28)\right) + a_3\ h_0 + a_4\ \cos\theta, \tag{163}$$

where θ_d is the latitude of the station, in degrees, and doy is the decimal day of year (UTC day since the beginning of the year). The coefficients in Eq. (163) are different with those in Eq. (122) as the later one is derived based on microwave refractivity index, which is independent on frequency.

These mapping functions along with the zenith delay model of Mendes and Pavlis (2004) have become the standard model for correcting SLR measurements. Comparing to the previously used mapping functions, the advantages of the new mapping functions are obvious. They represent simpler expressions than those proposed by the Marini and Murray (1973) model and allow the use of better zenith delay models. The coefficients of the mapping functions are presented in Table 6.

The latest progress in atmospheric corrections for single-color SLR is provided by Hulley and Pavlis (2007) who applied a ray-tracing technique to calculate propagation effects, including the effects of horizontal refractivity gradients. The use of ray-tracing trough numerical weather models has been shown to improve the accuracy of the SLR results.

4.3.2 Two-Color SLR Observations

The alternative to modeling is the application of two-color (i.e. two-frequency) SLR measurements for the direct computation of the propagation delay by utilizing the fact that the neutral atmosphere is dispersive for optical frequencies. The dispersion causes the optical path lengths at two different frequencies to differ. This difference depends on the two frequencies and is proportional to the path integrated atmospheric density. Thus, the difference between the two optical paths can be used for calculating the propagation delays (Wijaya and Brunner 2011). This method has the potential to improve the accuracy of SLR results (Abshire and Gardner 1985).

Based on the previous works of Prilepin (1957) and Bender and Owens (1965), Abshire and Gardner (1985) developed an atmospheric correction formula for the

Table 6 Coefficients (a_i, b_i, and c_i) for FCULa and FCULb mapping functions (Mendes et al. 2002)

	FCULa	FCULb
a_0	$(12100.8 \pm 1.9) \times 10^{-7}$	$(11613.1 \pm 1.6) \times 10^{-7}$
a_1	$(1729.5.8 \pm 4.3) \times 10^{-9}$	$(-933.8 \pm 9.7) \times 10^{-8}$
a_2	$(319.1 \pm 3.1) \times 10^{-7}$	$(-595.8 \pm 4.1) \times 10^{-11}$
a_3	$(-1847.8 \pm 6.5) \times 10^{-11}$	$(-2462.7 \pm 6.8) \times 10^{-11}$
a_4	–	$(1286.4 \pm 2.2) \times 10^{-7}$
b_0	$(30496.5 \pm 6.6) \times 10^{-7}$	$(29814.1 \pm 4.5) \times 10^{-7}$
b_1	$(234.6 \pm 1.5) \times 10^{-8}$	$(-56.9 \pm 2.7) \times 10^{-7}$
b_2	$(-103.5 \pm 1.1) \times 10^{-6}$	$(-165.5 \pm 1.1) \times 10^{-10}$
b_3	$(-185.6 \pm 2.2) \times 10^{-10}$	$(-272.5 \pm 1.9) \times 10^{-10}$
b_4	–	$(302.0 \pm 5.9) \times 10^{-7}$
c_0	$(6877.7 \pm 1.2) \times 10^{-5}$	$(68183.9 \pm 9.1) \times 10^{-6}$
c_1	$(197.2 \pm 2.8) \times 10^{-7}$	$(93.5 \pm 5.4) \times 10^{-6}$
c_2	$(-345.8 \pm 2.0) \times 10^{-5}$	$(-239.4 \pm 2.3) \times 10^{-9}$
c_3	$(106.0 \pm 4.2) \times 10^{-9}$	$(30.4 \pm 3.8) \times 10^{-9}$
c_4	–	$(-230.8 \pm 1.2) \times 10^{-5}$

two-color SLR measurements (the 2C-SLR formula). This formula was later studied by several investigators (Greene and Herring 1986).

From the two-color SLR measurements theoretical path lengths $\mathscr{R}_1$ and $\mathscr{R}_2$ are obtained (assume that the system measures simultaneously individual optical paths). With the 2C-SLR formula (Abshire and Gardner 1985), the chord (straight line) distance σ can be calculated by adding the term $\mu(\mathscr{R}_2 - \mathscr{R}_1)$ to $\mathscr{R}_1$

$$\sigma = \mathscr{R}_1 + \mu(\mathscr{R}_1 - \mathscr{R}_2), \tag{164}$$

where

$$\mu = \frac{k(\nu_1)}{k(\nu_2) - k(\nu_1)}, \tag{165}$$

with $k(\nu_i)$ being the dispersion factor. This factor depends on frequency and can be calculated using (Edlén 1966; Abshire and Gardner 1985)

$$k(\nu_i) = 0.9650 + \frac{0.0164}{\lambda_i^2} + \frac{0.000228}{\lambda_i^2}, \tag{166}$$

where λ_i is the i:th wavelength in meters.

The 2C-SLR formula presented in Eq. (164) remove the largest part of the total propagation delay, namely that associated with the dry atmospheric density. However, the water vapor density and curvature effects still remain (Abshire and Gardner 1985;

Greene and Herring 1986). At optical frequencies, water vapor contributes only about 1 % of the refractivity, however, since it is highly variable and it can introduce substantial errors. By using ray-tracing through atmospheric profiles, Wijaya and Brunner (2011) showed that the zenith wet delay can be several millimeters for SLR measurements. Furthermore, the magnitude of the bending effects could reach a few centimeters for measurements taken at an elevation angle of 10°.

The precision required for the range difference $(\mathscr{R}_1 - \mathscr{R}_2)$ measurements is very stringent (few micrometers), which is mainly due to amplification of the measurement noise by the scaling factor μ (Abshire and Gardner 1985; Greene and Herring 1986). This requirement cannot currently be achieved. However, if in the future the range difference measurements could be improved to reach the required precision, the two-color SLR system would be an interesting way of reduce atmospheric propagation effects.

In order to anticipate possible future development of the two-color SLR systems, Wijaya and Brunner (2011) have developed a new correction formula that can be seen as an extension of the 2C-SLR formula

$$\sigma = \mathscr{R}_1 + \mu(\mathscr{R}_1 - \mathscr{R}_2) + (\nu P_{21} - \kappa_1) + H_{21} \cdot \text{SIWV}. \tag{167}$$

The power of dispersion μ is given by

$$\mu = \frac{\tilde{k}_d(\nu_1)}{\tilde{k}_d(\nu_2) - \tilde{k}_d(\nu_1)}, \tag{168}$$

and the water vapor factor is

$$H_{21} = 10^{-6}\tilde{k}^{\star}_w(\nu_1)\nu\, K, \tag{169}$$

where $K = \left(\frac{\tilde{k}^{\star}_w(\nu_2)}{\tilde{k}^{\star}_w(\nu_1)} - \frac{\tilde{k}_d(\nu_2)}{\tilde{k}_d(\nu_1)}\right)$. The slant integrated water vapor (SIWV) is

$$\text{SIWV} = \int_{S_1} \rho_v(\mathbf{r}_1)\, \mathrm{d}s_1. \tag{170}$$

The formula in Eq. (167) eliminates the total atmospheric density effect including its gradient and provides two terms to calculate the water vapor and the curvature effects. The dispersion effect (contained in the second term in Eq. (167)) can be obtained from the observed optical path length difference $(\mathscr{R}_1 - \mathscr{R}_2)$. The third term represents the curvature effect of the ray path S_1 and the propagation corrections from S_2 to S_1. The last term represents the effects of the water vapor density. The constant μ represent the power of the dispersion effects and the constant H_{21} is the scaling factor for the wet delays. Both of these coefficients only dependent on the frequencies of the optical signals and can be calculated using Eqs. (168) and (169). The new formula, Eq. (167), is a general expression for the atmospheric correction

of two-color SLR measurements. When the water vapor and the curvature effects are neglected, the new formula reduces to the 2C-SLR formula, Eq. (164). Further detail of this new formula can be found in Wijaya and Brunner (2011).

4.4 Water Vapor Radiometry

A Water Vapor Radiometer (WVR) is an instrument that can be used to estimate the atmospheric wet delay. It does this by measuring the thermal radiation from the sky at microwave frequencies where the atmospheric attenuation due to water vapor is relatively high. These measurements can then be related to the wet delay.

Equation (9) describes the attenuation of radio signals caused by the atmosphere. The attenuation will depend upon frequency, as well as on temperature, pressure, humidity, and liquid water content. For details about how α can be modeled as function of these quantities, see e.g. Liebe et al. (1993) and Rosenkranz (1998).

Normally the radiation power from the sky is expressed using the brightness temperature T_B, which is defined as the physical temperature a black body would have if it radiates the same amount of power as the sky. For low frequencies T_B is related to W_{sky} by

$$W_{sky}(\nu) = k_b\, T_B(\nu)\, B, \tag{171}$$

where k_b is Bolzmann's constant and B the observed bandwidth. This relation is valid for frequencies $\nu \ll k_b T/h$, where h is Planck's constant. This requirement is fulfilled at microwave frequencies for normal atmospheric conditions.

The brightness temperature can be calculated from the equation of radiative transfer

$$T_B(\nu) = T_{bg}\, e^{-\tau(\infty,\nu)} + \int_S T(s)\, \alpha(s,\nu)\, e^{-\tau(s,\nu)}\, \mathrm{d}s, \tag{172}$$

where T_{bg} is the brightness temperature of the cosmic microwave background ($\approx$2.7 K). The opacity $\tau(s,\nu)$ is given by

$$\tau(s,\nu) = \int_0^s \alpha(s',\nu)\, \mathrm{d}s'. \tag{173}$$

T_B depends upon the pressure, temperature, humidity, and liquid water density profiles. The dependencies on these quantities will vary with frequency; for some frequencies (e.g. close to the center of a water vapor absorption line like 22.235 or 183 GHz) there will be a high sensitivity to water vapor while other frequencies (e.g. close to the center of the oxygen absorption lines around 60 and 120 GHz) are more sensitive to the pressure and temperature. For good sensitivity to these parameters, the attenuation needs to be high but not too high. If the attenuation is too high the brightness temperature will approach the physical temperature of the atmosphere, thus the sensitivity to the atmospheric properties will be lost. For retrieval of the

water vapor content the frequencies close to the 22.235 GHz line are normally the most suitable ones since this line is not too strong. For very dry conditions (e.g. high altitudes) higher frequencies (e.g. 183 GHz) will give higher sensitivity, however for normal conditions the attenuation is too high.

The sensitivity to the different atmospheric quantities also varies with height, e.g. some frequencies have a higher sensitivity to humidity close to the ground (frequencies on the edge of a water vapor absorption line) while others are more sensitive to the humidity at high altitudes (frequencies close to a water vapor absorption line). Thus it is in principle possible to estimate the humidity profile using radiometer measurements at several different frequencies having different sensitivity to humidity with height, a so-called radiometric profiler (Askne and Westwater 1986; Scheve and Swift 1999). This humidity profile could then be taken to calculate the tropospheric delay. However, the need for using many channels makes the radiometric profilers expensive, and it is difficult to find a set of frequencies from which the humidity profile can be estimated without running into any singularity problems. Furthermore, if only the integrated amount of water vapor—or the wet delay—is of interest we do not necessarily need to know the profile. If a frequency can be found where the sensitivity to the refractivity is constant with height, this is sufficient.

Normally the brightness temperature is not used directly to estimate the wet delay. Instead the opacity $\tau(\infty, \nu)$ is calculated from the brightness temperature, which is then used for the wet delay estimation. By introducing the effective temperature of the atmosphere T_{eff}

$$T_{eff}(\nu) = \frac{\int_S T(s)\,\alpha(s,\nu)\,e^{-\tau(s,\nu)}\,\mathrm{d}s}{\int_S \alpha(s,\nu)\,e^{-\tau(s,\nu)}\,\mathrm{d}s}, \tag{174}$$

we can write T_B as

$$T_B(\nu) = T_{bg}\,e^{-\tau(\infty,\nu)} + T_{eff}(\nu)\left(1 - e^{-\tau(\infty,\nu)}\right). \tag{175}$$

Thus the opacity can be estimated by

$$\tau(\infty,\nu) = -\ln\left[\frac{T_{eff} - T_B}{T_{eff} - T_{bg}}\right]. \tag{176}$$

Some WVR retrieval algorithms to estimate the wet delay from τ directly (Westwater et al. 1989; Bosisio and Mallet 1998). However, this requires that the effective temperature T_{eff} is accurately estimated. An alternative way is to use the linearized brightness temperature T_B' (Wu 1979)

$$T_B'(\nu) = T_{bg}\,[1 - \tau(\infty,\nu)] + \int_S T(s)\,\alpha(s,\nu)\,\mathrm{d}s. \tag{177}$$

The linearized brightness temperature can be calculated from the opacity by

$$T'_B(\nu) = T_{bg} + \left(T'_{eff}(\nu) - T_{bg}\right)\tau(\infty, \nu), \tag{178}$$

where the linearized effective temperature T'_{eff} is given by

$$T'_{eff}(\nu) = \frac{\int_S T(s)\,\alpha(s, \nu)\,\mathrm{d}s}{\tau(\infty, \nu)}. \tag{179}$$

If T_{eff} and T'_{eff} are consistently modeled, the error in T'_B caused by an error in T_{eff} will be approximately canceled by the error in T'_{eff}. Thus the linearized brightness temperature can normally be estimated with higher accuracy than the opacity.

The linearized brightness temperature can be divided into four parts

$$T'_B(\nu) = T_{bg} + T'_{wv} + T'_{lw} + T'_{ox}, \tag{180}$$

where T'_{wv}, T'_{lw}, and T'_{ox} are the contributions from water vapor, liquid water, and oxygen, respectively. T_{bg} is constant and well known. The oxygen part can be accurately modeled using measurements of the surface pressure and temperature (Jarlemark 1997), while the liquid water contribution is approximately proportional to the frequency squared (if the water droplets are much smaller than the wavelength). If the frequencies are properly chosen, T'_{wv} is proportional to the wet delay. Thus the wet delay can be estimated by a combination of measurements at two different frequencies ν_1 and ν_2

$$\Delta L_w = c_b \left[\left(\frac{\nu_2}{\nu_1}\right)^2 T'_B(\nu_1) - T'_B(\nu_2) - T_{bg,ox} \right], \tag{181}$$

where $T_{bg,ox}$ is the contribution from oxygen and the cosmic microwave background.

For the estimation of the wet delay we need to know the retrieval coefficient c_b, as well as $T_{bg,ox}$, T_{eff}, and T'_{eff}. Normally these parameters are modeled as functions of the surface pressure, temperature, and humidity. To model c_b, one can use WVR measurements and simultaneous observations of the wet delay made by another instruments. Then the model coefficients can be obtained by fitting the radiometer observations to the wet delay observations. The disadvantage of this method is that it requires a long time series of measurements, ideally longer than one year in order to be able to take seasonal variations into account. Furthermore, any systematic error in the wet delay measurements will cause systematic errors in the retrieval coefficient. A more commonly used method is to use profiles of pressure, temperature and humidity obtained from e.g. radiosondes to calculate the theoretical values of T'_B, $T_{bg,ox}$, T_{eff}, T'_{eff}, and ΔL_w. These can then be used to estimate appropriate models for the parameters. For details, see e.g. Elgered (1993) and Jarlemark (1997).

Several studies have been performed where WVRs have been used to correct for the wet tropospheric delays in space geodetic (mostly VLBI) data analysis. Examples of such studies are Elgered et al. (1991), Kuehn et al. (1991), Ware et al. (1993),

Emardson et al. (1999) and Nothnagel et al. (2007). The results indicate that the accuracy of the VLBI estimates can be improved if WVRs are used to calibrate the tropospheric delay compared to the normal method of estimating the tropospheric delay as function in the data analysis (see Sect. 4.2), although the results are inconclusive. It should be noted that the WVR calibration was only applied at a few sites since most VLBI stations are not equipped with radiometers. One problem with radiometers is that they cannot be used during rain for several reasons (liquid water on radiometer antenna, saturation problems, water droplets may not be "small", …). Furthermore, most radiometer antennas have relatively large beam-widths (several degrees), and thus the observations are limited to high elevation angles (>15–20°) in order to avoid picking up radiation from the ground. Hence, either VLBI observations made at low elevation angles have to be excluded, or the WVR measurements need to be extrapolated to low elevation angles, which is a process that can introduce errors.

5 Atmospheric Turbulence

The normal modeling of atmospheric delays in space geodesy, i.e. using mapping functions and horizontal gradients assumes that the spatial variations in the refractivity are linear, and that the temporal variations can be described by e.g. piece-wise linear functions. For the large-scale variations this is an adequate approximation, however at small scales there are non-linear variations caused by atmospheric turbulence. Although it is normally impossible to correct for these random fluctuations, it can be important to model them in order to minimize their effect on the results.

Atmospheric turbulence occurs when energy from e.g. wind shears and temperature gradients creates turbulent eddies. These eddies then break down into smaller eddies until at very small scales the energy of the eddies are dissipated into heat. Inside each eddy the air is mixed, and thus large-scale variations in any atmospheric quantity, e.g. refractivity, will be mixed to create random small-scale variations.

A turbulent eddy with a size R will have a characteristic wind velocity v. Kolmogorov (1941a, b) assumed that the rate of which kinetic energy (per unit mass) of an eddy is transferred to smaller eddies is only dependent on R and v. By dimensional analysis it is clear that this rate must be proportional to v^3/R. For stationary turbulence the kinetic energy for the eddies of a specific size will be constant, i.e. the kinetic energy received from larger eddies must be equal to the energy lost to smaller scale eddies (assuming no dissipation into heat at larger scale). At small scales the kinetic energy is dissipated into heat with a dissipation rate ε, which thus must be equal to the kinetic energy rate of all larger eddies. Thus $v \propto \varepsilon^{1/3} R^{1/3}$, or equivalently that the structure function for the velocity fluctuations between $\mathbf{r}$ and $\mathbf{r} + \mathbf{R}$ is given by

$$D_v(\mathbf{R}) = \left\langle [\mathbf{v}(\mathbf{r}) - \mathbf{v}(\mathbf{r} + \mathbf{R})]^2 \right\rangle = C_v^2 \varepsilon^{2/3} \, \|\mathbf{R}\|^{2/3} \,, \tag{182}$$

where C_v is the velocity structure constant.

It can be shown that the structure functions for other atmospheric variables, like the temperature and the refractive index, are similar (i.e. also proportional to $\|\mathbf{R}\|^{2/3}$). Thus the fluctuations in refractive index between two locations, $\mathbf{r}$ and $\mathbf{r}+\mathbf{R}$, can be described by the structure function $D_n(\mathbf{R})$

$$D_n(\mathbf{R}) = \left\langle [n(\mathbf{r}) - n(\mathbf{r}+\mathbf{R})]^2 \right\rangle = C_n^2 \, \|\mathbf{R}\|^{2/3} . \tag{183}$$

The constant C_n^2 is called the refractive index structure constant. This equation is however not valid for large scales since it becomes infinite when the distance approaches infinity, which is unrealistic. In order to fix this problem, Treuhaft and Lanyi (1987) modified the expression by introducing a saturation length scale L

$$D_n(\mathbf{R}) = \left\langle [n(\mathbf{r}) - n(\mathbf{r}+\mathbf{R})]^2 \right\rangle = C_n^2 \frac{\|\mathbf{R}\|^{2/3}}{1 + \left[\dfrac{\|\mathbf{R}\|}{L} \right]^{2/3}} . \tag{184}$$

With this expression $D_n(\mathbf{R})$ will converge to $C_n^2 L^{2/3}$ as $\|\mathbf{R}\|$ goes to infinity.

Turbulence does not only cause spatial variations in the refractive index, but also temporal variations. One way to describe the temporal variations is to assume Taylor's frozen flow hypothesis (Taylor 1938). In this hypothesis the turbulent variations in the refractive index in the atmosphere are frozen and move with the wind velocity $\mathbf{v}$, i.e. it is assumed that $n(\mathbf{r}, t) = n(\mathbf{r} - \mathbf{v}(t - t_0), t_0)$. This is an approximation which works well over shorter time periods but may not be valid over longer time periods (hours, days). By using Taylor's frozen flow hypothesis the temporal variations in the refractive index over a time period T can be d escribed by the structure function $D_n(T)$

$$D_n(T) = \left\langle [n(t) - n(t+T)]^2 \right\rangle = C_n^2 \frac{[\|\mathbf{v}\| \, T]^{2/3}}{1 + \left[\dfrac{\|\mathbf{v}\| \, T}{L} \right]^{2/3}} . \tag{185}$$

By combining Eqs. (184) and (185) we get a general expression for the structure function for the fluctuations in the refractive index between $\mathbf{r}_1$ at time t_1 and $\mathbf{r}_2$ at time t_2

$$D_n(\mathbf{r}_1, t_1; \mathbf{r}_2, t_2) = \left\langle [n(\mathbf{r}_1, t_1) - n(\mathbf{r}_2, t_2)]^2 \right\rangle = C_n^2 \frac{[\|\mathbf{r}_1 - \mathbf{r}_2 - \mathbf{v}(t_1 - t_2)\|]^{2/3}}{1 + \left[\dfrac{\|\mathbf{r}_1 - \mathbf{r}_2 - \mathbf{v}(t_1 - t_2)\|}{L} \right]^{2/3}} . \tag{186}$$

5.1 Turbulence Effects on Tropospheric Delays

For the modeling of the effects of turbulence on tropospheric delays we make two assumptions. First that the geometric optics approximation is still valid, i.e. that the turbulent variation within one wavelength can be ignored. Furthermore, we assume that there is no effect on the propagation path of the signal. Both these assumption can be considered approximately valid for weak turbulence. For the case of very strong turbulence more advanced considerations need to be made, see e.g. Tatarskii (1971) and Ishimaru (1978).

The fluctuations in the refractive index will cause variations in the atmospheric delays of radio signals; both in time and as function of direction and location. When describing these fluctuations it is convenient to work with the *Equivalent Zenith Tropospheric Delay* (EZTD) instead of the slant delays. The EZTD ΔL^z is the slant tropospheric delay divided by a symmetric mapping function *mf*

$$\Delta L^z(e,a,t) = \frac{\Delta L(e,a,t)}{mf(e)} = \int_0^\infty [n(\mathbf{r}(z),t) - 1]\, \mathrm{d}z, \tag{187}$$

where e is the elevation angle, a is the azimuth angle, and $\mathbf{r}(z)$ denotes the position of the ray at height z.

The structure function between two EZTD, observed at two different times in two different directions and possibly from two different locations, can be calculated by:

$$\begin{aligned} D_L &= \left\langle \left[\Delta L_1^z - \Delta L_2^z\right]^2 \right\rangle \qquad (188)\\ &= \left\langle \left(\int_0^\infty [n(\mathbf{r}_1(z),t_1) - 1]\, \mathrm{d}z - \int_0^\infty [n(\mathbf{r}_2(z),t_2) - 1]\, \mathrm{d}z \right)^2 \right\rangle \\ &= \int_0^\infty \int_0^\infty \Big[\left\langle n(\mathbf{r}_1(z),t_1)\, n(\mathbf{r}_1(z'),t_1) \right\rangle + \left\langle n(\mathbf{r}_2(z),t_2)\, n(\mathbf{r}_2(z'),t_2) \right\rangle \\ &\qquad \left\langle n(\mathbf{r}_1(z),t_1)\, n(\mathbf{r}_2(z'),t_2) \right\rangle + \left\langle n(\mathbf{r}_2(z),t_2)\, n(\mathbf{r}_1(z'),t_1) \right\rangle \Big]\, \mathrm{d}z\, \mathrm{d}z' \,. \end{aligned}$$

Using the relation $A \cdot B = 0.5(A^2 + B^2 - (A-B)^2$, this simplifies to

$$\begin{aligned} D_L = \int_0^\infty \int_0^\infty \Big[& D_n(\mathbf{r}_1(z),t_1;\mathbf{r}_2(z'),t_2) - \frac{1}{2} D_n(\mathbf{r}_1(z),t_1;\mathbf{r}_1(z'),t_1) \qquad (189)\\ & - \frac{1}{2} D_n(\mathbf{r}_2(z),t_2;\mathbf{r}_2(z'),t_2) \Big]\, \mathrm{d}z\, \mathrm{d}z'. \end{aligned}$$

With the expression for D_n given by Eq. (186), the structure function D_L can be calculated.

Figure 14 shows the structure function $D_L(\rho)$ for spatial variations in the zenith wet delay as function of the distance ρ. In the calculations it was assumed that $C_n^2 = 1 \cdot 10^{-14}\ \mathrm{m}^{-2/3}$ up to a height of $H = 2$ km and zero above, and $L = 3000$ km.

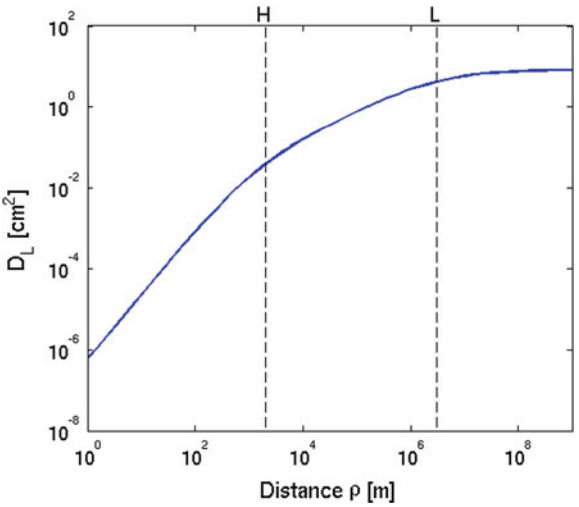

Fig. 14 The spatial structure function D_L (Eq. 186) for the zenith wet delay

We can here note three regions: for $\rho \ll H$ we have $D_L(\rho) \propto \rho^{5/3}$, for $H \ll \rho \ll L$ we have $D_L(\rho) \propto \rho^{2/3}$, and for $\rho \gg L$ we $D_L(\rho) \approx C_n^2 H^2 L^{2/3}$ (i.e. constant).

From he structure function D_L the covariance matrix for the turbulent fluctuations in the tropospheric delay can be calculated. This can then be applied to weight the observations in the estimation procedure. For more details, see e.g. Treuhaft and Lanyi (1987). It is also possible to use D_L for simulating tropospheric delays, see e.g. Nilsson and Haas (2010).

5.2 Estimating C_n^2

In order to calculate the structure function D_L the profile of the structure constant C_n^2 needs to be known. This parameter is highly variable, both in time and between different locations. Several methods to determine C_n^2 exist, see Nilsson and Haas (2010) for a review of some of them.

One way to determine C_n^2 is to use observations of variations in the tropospheric delay. For example, C_n^2 can be estimated from the observed variations of the tropospheric delay between different directions (Nilsson et al. 2005) or between different locations (Treuhaft and Lanyi 1987). Here we describe how to estimate C_n^2 from observations of the zenith delay variance over a time period T

$$\sigma_L^2(T) = \left\langle \frac{1}{T} \int_0^T \left[\Delta L^z(t + t_0) - \frac{1}{T} \int_0^T L^z(t' + t_0)\, \mathrm{d}t' \right]^2 \mathrm{d}t \right\rangle. \tag{190}$$

After some calculations, it can be shown that (Treuhaft and Lanyi 1987)

$$\sigma_L^2(T) = \frac{1}{T^2} \int_0^T (T - t)\, D_L(t)\, \mathrm{d}t. \tag{191}$$

In order to estimate C_n^2 using observations of σ_L^2 we need to know the shape of the C_n^2 profile. When we want to estimate a C_n^2 that can be used for calculating D_L it is however not critical to know the exact shape of the profile, most important is then that the integrated value of C_n^2 is correct. Thus we can for example make the approximation that C_n^2 has an exponential profile or, even more simple, assume that C_n^2 is constant up to a height H and zero above as done by Treuhaft and Lanyi (1987). Using the latter approximation, C_n^2 at heights lower than H can be calculated from

$$C_n^2 = \frac{\sigma_L^2(T)}{\int_0^T (T - t) \int_0^H \int_0^H \left\{ \left[(z - z')^2 + (v\, t)^2 \right]^{1/3} - |z - z'|^{2/3} \right\} \mathrm{d}z\, \mathrm{d}z'\, \mathrm{d}t}. \tag{192}$$

The height H should be chosen such that the largest fluctuations in the refractive index occur below H. For microwaves where the fluctuations in the wet delay is dominating an appropriate choice is the scale height of water vapor (approximately 2 km).

Another possible way to obtain C_n^2 is to use vertical profiles of pressure, temperature, and humidity obtained from e.g. radiosonde measurements. As discussed above, when turbulence is present, large-scale variations (gradients) in the atmosphere are mixed and create small-scale fluctuations. Thus there will be variations caused by both the large-scale gradients as well as turbulence. At large scales the variations due to gradients will dominate, and at small scales turbulence. At some scale in between the magnitudes of the large-scale gradients and by turbulence will be equal. This scale is proportional to the so-called *outer scale of turbulence* L_0. Typically values of L_0 range between a few meters to several hundreds of meters. The value can vary with time, but for the calculations of C_n^2 typically a mean value is used (d'Auria et al. 1993). Hence

$$C_n^2\, L_0^{2/3} \propto \|\nabla n\|^2\, L_0^2. \tag{193}$$

Thus C_n^2 could be calculated from the gradient in n. Since the gradient of the refractive index is typically more than one order of magnitude larger in the vertical direction than in the horizontal direction, we can approximate the refractive index gradient by its vertical component. However, one problem that needs to be considered is that the refractive index is not conserved in adiabatic motion in the atmosphere. When an air parcel is moved up or down in the atmosphere (e.g. due to turbulence) its size will change due to the change of atmospheric pressure with height. This in turn will cause the temperature and partial pressure of water vapor—and thus also the refractivity—to change. This needs to be corrected for when calculating C_n^2. The way to do this is to consider the vertical gradient in the refractive index caused by vertical gradients in quantities conserved under adiabatic motion in the atmosphere, e.g. the potential

temperature θ and the specific humidity q

$$\theta = T\left(\frac{p_0}{p}\right)^{0.286}, \tag{194}$$

$$q = \frac{p_w}{1.62p}, \tag{195}$$

where p_0 =1000 hPa. Thus C_n^2 can be calculated as

$$C_n^2 = a^2 L_0^{4/3}\left[\frac{\partial n}{\partial \theta}\frac{\partial \theta}{\partial z} + \frac{\partial n}{\partial q}\frac{\partial q}{\partial z}\right]^2, \tag{196}$$

where a^2 is a constant ($a^2 \approx 2.8$ (d'Auria et al. 1993)). The vertical gradients should not contain any variations due to turbulence, thus they should be evaluated over height intervals larger than L_0.

Equation (196) is however only valid if there is turbulence present. When no turbulence is present C_n^2 should be (close to) zero. One way to determine if the air is turbulent or not is to use the Richardson number Ri (Richardson 1920)

$$Ri = \frac{g}{\theta}\frac{\partial \theta}{\partial z}\left\|\frac{\partial \mathbf{v}}{\partial z}\right\|^{-2}. \tag{197}$$

The atmosphere is turbulent when Ri is larger than a critical Richardson number Ri_c, typically $Ri_c \approx 0.25$. Thus Eq. (196) modifies to

$$C_n^2 = a^2 L_0^{4/3} F\left[\frac{\partial n}{\partial \theta}\frac{\partial \theta}{\partial z} + \frac{\partial n}{\partial q}\frac{\partial q}{\partial z}\right]^2, \tag{198}$$

where $F = 1$ if $Ri < Ri_c$ and zero otherwise. This is however still a bit too simplistic since this assumes a very sharp transition between a turbulent and a non-turbulent state. d'Auria et al. (1993) presented a model for F giving a more smooth transition between 0 and 1 around Ri_c.

6 Applications of Space Geodetic Techniques for Atmospheric Studies

As discussed earlier, it is important to have a good model of the delay in the neutral atmosphere in order to obtain the highest accuracy in the space geodetic results (e.g. station positions). Since external estimates of the wet delay with high enough accuracy are typically not available (at least for microwave techniques), the common way of handling the wet delay in the data analysis is to estimate it, i.e. by modeling it using mapping functions and gradients as described in Sect. 4.2. Thus the results of

the data analysis will also contain information about the tropospheric delay, which is closely related to the IWV (see Sect. 3.2.2). Several studies investigated the accuracy of the zenith wet delays and IWV estimated from VLBI and GNSS (e.g. Herring et al. 1990, Tralli and Lichten 1990, Bevis et al. 1992, Snajdrova et al. 2006, Teke et al. 2011), and these show that it is on the same level or better then that of other techniques. Thus there exists a large interest in applying space geodetic techniques, especially GNSS, for atmospheric studies. For example, zenith wet delays can be used to study climate trends (Sect. 6.1), or assimilated into numerical weather prediction models to improve weather forecasts (Sect. 6.2). With wet delays estimated from a local GNSS network one can even attempt to estimate the 3D structure of the atmospheric water vapor by applying tomographic methods (Sect. 6.3).

6.1 Long-Term Water Vapor Trends

Since the zenith wet delay is closely related to the integrated water vapor content (see Sect. 3.2.2), we can analyze ΔL_w^z estimated from space geodetic techniques to study the variations of the atmospheric water vapor content in time. For example, it is possible to study diurnal and seasonal variations as well as long term trends in the water vapor content. Such information is of great interest in climatology since the water vapor content is closely related to the temperature. Climate models typically predict that the average relative humidity remains constant as the temperature changes (Trenberth et al. 2003). Since the saturation water vapor pressure depends approximately exponentially on the temperature, this means that a a change in the temperature will cause a corresponding change in the water vapor content. It is predicted that an increase in temperature of 1 K will increase the water vapor content by 6–7 % (Trenberth et al. 2003; Bengtsson et al. 2004). It is important to monitor the water vapor content since water vapor is a greenhouse gas, in fact the most important one. Additionally, higher water vapor content can also indicate an intensified hydrological cycle, including increased precipitation.

Several studies have calculated long-term trends in ΔL_w^z (or IWV) estimated from GNSS and VLBI, e.g. Gradinarsky et al. (2002); Jin et al. (2007); Steigenberger et al. (2007); Heinkelmann et al. (2007); Ning and Elgered (2012). An example of ΔL_w^z trends calculated from ten years of GPS data in Sweden and Finland is shown in Fig. 15. For more details, see Nilsson and Elgered (2008).

6.2 GNSS Meteorology

Water vapor is a very important parameter in meteorology and in order to get accurate weather forecasts it is very important to have accurate measurements of the water vapor content. A problem is that the water vapor content is highly variable in both space and time, and traditional instruments (e.g. radiosondes) do not pro-

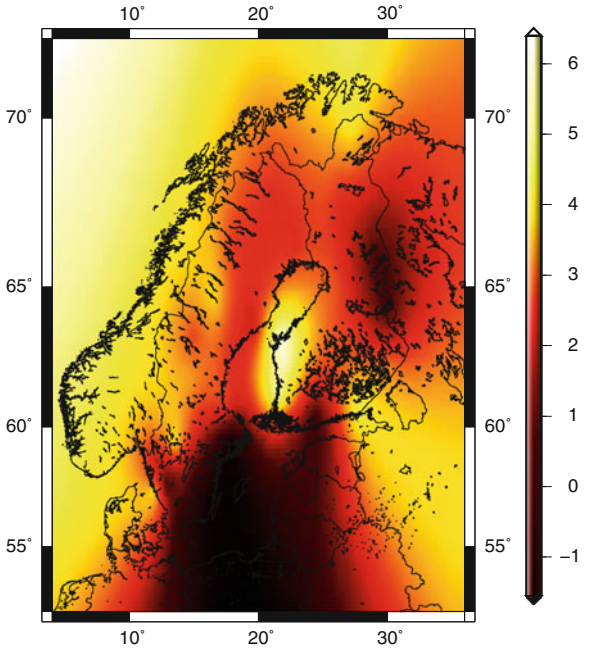

Fig. 15 Zenith wet delay trends in mm/decade estimated from GPS data in Sweden and Finland, 1997–2006. Modified from Nilsson and Elgered (2008)

vide the water vapor content with high enough spatial and temporal resolution. With the establishment of relative dense GNSS networks the meteorological community has started to be interested in assimilating zenith total delays or zenith wet delays estimated from these GNSS networks in the numerical weather prediction models (Gutman and Benjamin 2001; Poli et al. 2007).

Several investigations of assimilating GNSS tropospheric delays in numerical weather prediction models have been performed. For example, in Europe this has been investigated in the projects COST-716 (Elgered et al. 2005), TOUGH (Vedel 2006), and E-GVAP (http://egvap.dmi.dk/). It has been shown that the quality of the forecasts improve if GNSS data are assimilated, especially in cases of high precipitation (Vedel and Huang 2004; Karabatić et al. 2011).

6.3 GNSS Tropospheric Tomography

Tomography is a method which can be used to estimate the 2D or 3D structure of a quantity from measurements of the integral of the quantity along different paths. It is a method commonly used in medicine, seismology, material science, and a number of other fields. Tomography can also be applied to atmospheric delay measurements

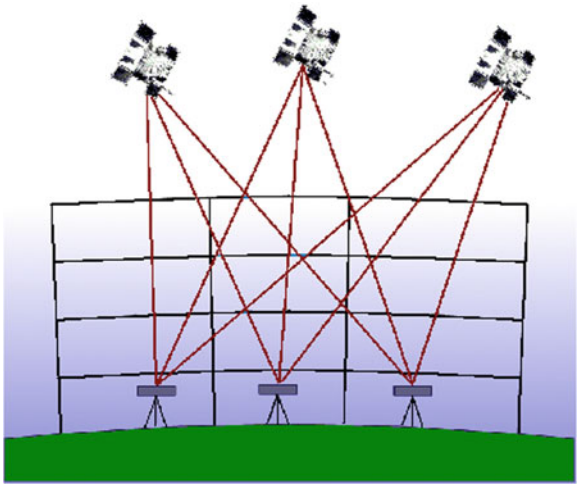

Fig. 16 Example of a GNSS tomography scenario. Note that for better visibility the relative size of the troposphere have been enlarged; in reality the troposphere (= top of highest voxel) is about 10 km heigh, the inter-station distances a few km, while the satellites are are at about 20000 km altitude

in order to reconstruct the 3D structure of the wet (or total) refractivity. This requires that the slant wet delays are measured by several stations in a local (inter-station distance maximum a few km) network. The only space geodetic technique for which such dense networks are available is GNSS.

A picture of a GNSS tomography scenario is shown in Fig. 16. In order to estimate the wet refractivity field from the observed wet delays, the atmosphere above the GNSS network is parameterized. The most commonly used parameterization is voxels, although other parameterizations are also possible (Perler et al. 2011). Voxel parameterization means that the atmosphere is divided into a number of boxes (called voxels, volume pixels) in which the refractivity is assumed constant. Thus the wet tropospheric delays along the rays of the observed GNSS signals can be described by a linear combination of the voxel refractivities

$$\Delta L_i = \sum_{j=1}^{n_{vox}} N_j \, D_{ij}. \tag{199}$$

ΔL_i is the wet tropospheric delay along the ith ray, n_{vox} is the number of voxels, N_j is the refractivity of the jth voxel, and D_{ij} is the distance traveled by ray i in voxel j. Since the station and satellite coordinates are normally known, D_{ij} can be calculated. Having observations of the tropospheric delays along several different rays, a linear system of equations is obtained

$$\Delta \mathbf{L} = \mathbf{DN}. \tag{200}$$

$\Delta\mathbf{L}$ and $\mathbf{N}$ are vectors containing the wet delays and the refractivities, respectively, and $\mathbf{D}$ is a matrix containing the D_{ij} values. By inverting the system, the voxel refractivities are estimated.

There are however a few problems with this method. One is how to estimate the slant wet delays along the GNSS signal rays. One way is to estimate the zenith wet delay and gradients in a normal GNSS analysis, then use these to calculate the slant wet delays. This is for example done by Champollion et al. (2005). However, this method will limit the accuracy since it assumes that all horizontal variations in the refractivity above a station are linear, something which is not always realistic. In order to improve the slant wet delays, it is often assumed that the post-fit residuals of the GNSS analysis will contain the unmodeled parts of the slant wet delays, and thus adding these to the calculated slant wet delays will give the true delays (Alber et al. 2000; Troller et al. 2006). This is not true, the residuals will contain also other errors of the GNSS measurements (e.g. multi-path). Another approach is to model the slant delays by using Eq. (199) in the GNSS data analysis instead of zenith delays and gradients. First results using this approach are presented by Nilsson and Gradinarsky (2006) and Nilsson et al. (2007).

Another problem is the normally weak geometry since tomography ideally requires that there are rays crossing the investigated volume in all possible directions. In GNSS tomography, however, all rays are going between the top of the troposphere to the stations on the surface of the Earth, while there are no rays entering and/or leaving the voxel grid at the sides. This makes the sensitivity to the vertical refractivity profile very low and as a result the equation system (200) will be ill-conditioned. This problem can be solved by either constraining the refractivity field to some a priori field obtained either by models or external measurements like radiosondes. The problem is not as big if the GNSS stations are placed at very different altitudes (e.g. if there are differences of several kilometers between highest and lowest stations) (Nilsson and Gradinarsky 2006).

Furthermore, since the satellite geometry will change during the day, some voxels may at times have no or only a few rays passing through it. Thus, in order to avoid singularity problems, constraints need to be applied. Simple constraints are for example inter-voxel constraints which constrain the refractivity of a voxel to the mean refractivity of the neighboring voxels (Flores et al. 2000). A more advanced approach is to use a Kalman filter with a covariance matrix for the voxel refractivity calculated from turbulence theory using Eq. (186) (Gradinarsky and Jarlemark 2004; Nilsson and Gradinarsky 2006).

Figure 17 shows the results of two simulations demonstrating the strengths and weaknesses of GNSS tomography. In the upper plot the case where the refractivity is 20 mm/km in the layer between 3 and 4 km altitude and zero elsewhere is simulated. As seen the tomographic reconstruction is not working well. This is because of the weak geometry in the vertical direction, resulting in a very low sensitivity to the height of the layer with non-zero refractivity. Thus the refractivity is spread out over all layers in the tomographic reconstruction. Most refractivity is put in the lower layers simply because the tomographic software is set up to allow for a higher variability in the refractivity at lower altitudes than at higher altitudes. The estimated refractivity

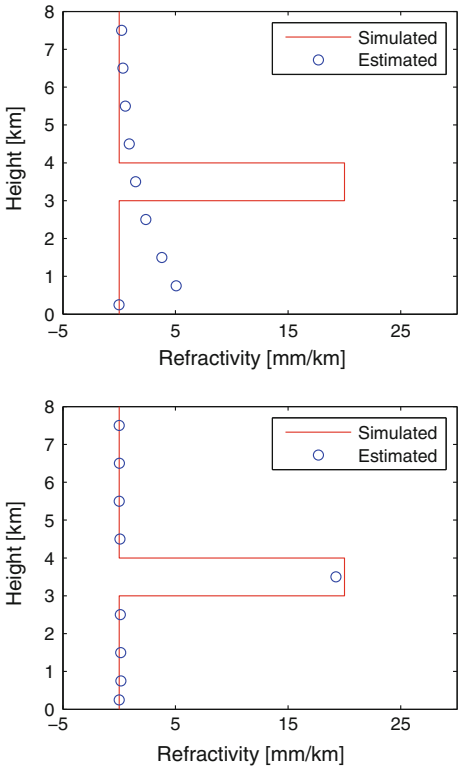

Fig. 17 Simulation results of tomographic reconstruction of the refractivity field. The *upper plot* shows the result obtained when the simulated refractivity field was 20 mm/km in the fifth layer and zero elsewhere. In the *lower plot* the simulated refractivity field is 20 mm/km only in the middle voxel of the fifth layer, and zero elsewhere. These results are from Nilsson (2007)

in the lowest layer is however correctly estimated to zero. Here the sensitivity is higher since the stations are at slightly different altitudes. In the lower plot of Fig. 17 the simulated refractivity field is non-zero just in one voxel: the middle voxel (of 25) of the layer between 3 and 4 km. In this case the tomographic reconstruction is working better. This demonstrates that GNSS tomography can have a good sensitivity to horizontal fluctuations in the refractivity field, and is even able to determine at which height these fluctuations are occurring. For more details about the simulation setup and other results from similar simulations, see Nilsson (2007).

Acknowledgments First of all we would like to thank the reviewer, Gunnar Elgered, for providing very valuable suggestions to improve the quality of this part of the book. We are grateful for the financial support from the German Science Foundation (DFG, SCHU 1103/3-2), and from the Austrian Science Fund (FWF, P20902-N10).

References

J. B. Abshire and C. S. Gardner. Atmospheric refractivity corrections in Satellite Laser Ranging. *IEEE Trans. Geosc. Rem. Sens.*, GE-23(4):414–425, 1985. doi:10.1109/TGRS.1985.289431.

C. Alber, R. Ware, C. Rocken, and J. Braun. Obtaining single path delays from GPS double differences. *Geoph. Res. Lett.*, 27:2661–2664, 2000. doi:10.1029/2000GL011525.

M. Alizadeh, D. D. Wijaya, T. Hobiger, R. Weber, and H. Schuh. Ionospheric effects on microwave signals. In *Atmospheric Effects in Space Geodesy*. Springer-Verlag, 2013. this book.

T. Alkhalifah and S. Fomel. Implementing the fast marching Eikonal solver: Spherical versus cartesian coordinates. *Geophys. Prospect.*, 49:165 178, 2001. doi:10.1046/j.1365-2478.2001.00245.x.

J. I. H. Askne and E. R. Westwater. A review of ground-based remote sensing of temperature and moisture by passive microwave radiometers. *IEEE Trans. Geosci. Remote Sensing*, GE-24 (3):340–352, 1986. doi:10.1109/TGRS.1986.289591.

B. R. Bean and G. D. Thayer. CRPL exponential reference atmosphere. Technical report, U.S. Government Printing Office, 1959. URL http://digicoll.manoa.hawaii.edu/techreports/PDF/NBS4.pdf.

P. L. Bender and J. C. Owens. Correction of optical distance measurements for the fluctuating atmospheric index of refraction. *J. Geophys. Res.*, 70:2461, 1965. doi:10.1029/JZ070i010p02461.

L. Bengtsson, S. Hagemann, and K. I. Hodges. Can climate trends be calculated from reanalysis data? *J. Geophys. Res.*, 109:D11111, 2004. doi:10.1029/2004JD004536.

H. Berg. *Allgemeine Meteorologie.* Dümmlers Verlag, Bonn, 1948.

M. Bevis, S. Businger, S. Chiswell, T. A. Herring, R. A. Anthes, C. Rocken, and R. H. Ware. GPS meteorology: Mapping zenith wet delays onto precipitable water. *J. Appl. Meteorology*, 33(3):379–386, 1994. doi:10.1175/1520-0450(1994)033<0379:GMMZWD>2.0.CO;2.

M. Bevis, S. Businger, T.A. Herring, C. Rocken, R.A. Anthes, and R.H. Ware. GPS meteorology: remote sensing of atmospheric water vapor using the global positioning system. *J. Geophys. Res.*, 97(D14):15787–801, 1992. ISSN 0148–0227. doi:10.1029/92JD01517.

J. Böhm. *Troposphärische Laufzeitverzögerungen in der VLBI.* PhD thesis, Technische Universität Wien, 2004.

J. Böhm, R. Heinkelmann, and H. Schuh. Short Note: A global model of pressure and temperature for geodetic applications.*J. Geodesy*, 81(10):679–683, OCT 2007. doi:10.1007/s00190-007-0135-3.

J. Böhm, R. Heinkelmann, and H. Schuh. Neutral atmosphere delays: Empirical models versus discrete time series from numerical weather models. In H. Drewes, editor, *Geodetic Reference Frames - IAG Symposium*, volume 134 of IAG Symposia, pages 317–321, Munich, Germany, 2009a. doi:10.1007/978-3-642-00860-3_49.

J. Böhm, J. Kouba, and H. Schuh. Forecast Vienna mapping functions 1 for real-time analysis of space geodetic observations. *J. Geodesy*, 83(5), 2009b. doi:10.1007/s00190-008-0216-y.

J. Böhm, P.J. Mendes Cerveira, H. Schuh, and P. Tregoning. The impact of mapping functions for the neutral atmosphere based on numerical weather models in GPS data analysis. In P. Tregoning and C. Rizos, editors, *Dynamic Planet, volume 130 of IAG Symposia Series*, pages 837–843. Springer-Verlag, 2007. doi:10.1007/978-3-540-49350-1_118.

J. Böhm, A. Niell, P. Tregoning, and H. Schuh. Global mapping function (GMF): a new empirical mapping function based on numerical weather model data. *Geophys. Res. Lett.*, 33:L07304, 2006a. doi:10.1029/2005GL025546.

J. Böhm, D. Salstein, M. Alizadeh, and D. D. Wijaya. Geodetic and atmospheric background. In *Atmospheric effects in space geodesy*. Springer-Verlag, Berlin, Germany, 2013. this book.

J. Böhm and H. Schuh. Vienna mapping functions. In *Proc. 16th Working Meeting on European VLBI for Geodesy and Astrometry*, page 131 143, Leipzig, Germany, 2003. Verlag des Bundesamtes für Kartographie und Geodäsie.

J. Böhm and H. Schuh. Vienna mapping functions in VLBI analyses. *Geophys. Res. Lett.*, 31:L01603, 2004. doi:10.1029/2003GL018984.

J. Böhm and H. Schuh. Tropospheric gradients from the ECMWF in VLBI analysis. *J. Geodesy,* 81(6–8):409–421, 2007. doi:10.1007/s00190-006-0126-9.

J. Böhm, B. Werl, and H. Schuh. Troposphere mapping functions for GPS and very long baseline interferometry from european centre for medium-range weather forecasts operational analysis data. *J. Geophys. Res.*, 111:B02406, 2006b. doi:10.1029/2005JB003629.

M. Born and E. Wolf. *Principles of optics*. Cambridge Univ. Press, New York, 7th edition, 1999.

A. V. Bosisio and C. Mallet. Infuence of cloud temperature on brightness temperature and consequences for water retrieval. *Radio Sci.*, 33(4):929–939, 1998. doi:10.1029/98RS00949.

G. Boudouris. On the index of refraction of air, the absorption and dispersion of centimeter waves in gases. *J. Res. Natl. Bur. Stand.*, 67D:631–684, 1963.

K. G. Budden. *The propagation of radio waves*. Cambridge University Press, New York, 1 edition, 1985.

V. Cerveny. *Seismic ray theory*. Cambridge University Press, New York, 2005.

V. Cerveny, L. Klimes, and I. Psencik. Complete seismic-ray tracing in three-dimensional structures. In D. J. Doornbos, editor, *Seismological algorithms*, page 89–168. Academic Press, New York, 1988.

C. Champollion, F. Mason, M.-N. Bouin, A. Walpersdorf, E. Doerflinger, O. Bock, and J. van Baelen. GPS water vapour tomography: preliminary results from the ESCOMPTE field experiment. *Atmospheric Research*, 74:253–274, 2005. doi:10.1016/j.atmosres.2004.04.003.

C.C. Chao. The troposphere calibration model for mariner mars 1971. Technical Report 32–1587, NASA JPL, Pasadena, CA, 1974.

G. Chen and T. A. Herring. Effects of atmospheric azimuthal asymmetry on the analysis of space geodetic data. *J. Geophys. Res.*, 102(B9):20489–20502, 1997. doi:10.1029/97JB01739.

P. E. Ciddor. Refractive index of air: new equations for the visible and near infrared. *Appl. Opt.*, 35(9):1566–1573, 1996. doi:10.1364/AO.35.001566.

P. E. Ciddor and R. J. Hill. The refractive index of air 2. Group index. *Appl. Opt.*, 38:1663–1667, 1999. doi:10.1364/AO.38.001663.

G. d'Auria, F. S. Marzano, and U. Merlo. Model for estimating the refractive-index stucture constant in clear-air intermittent turbulence. *Applied Optics*, 32:2674–2680, 1993. doi:10.1364/AO.32.002674.

J. L. Davis, G. Elgered, A. E. Niell, and C. E. Kuehn. Ground-based measurement of gradients in the "wet" radio refractivity of air. *Radio Sci.*, 28(6):1003–1018, 1993. doi:10.1029/93RS01917.

J. L. Davis, T. A. Herring, I. I. Shapiro, A. E. E. Rogers, and G. Elgered. Geodesy by radio interferometry: Effects of atmospheric modeling errors on estimates of baseline length. *Radio Sci.*, 20(6):1593–1607, 1985. doi:10.1029/RS020i006p01593.

J.L. Davis. Atmospheric propagation effects on radio interferometry. Technical Report AFGL-TR-86-0243, Scientific Report No. 1, Air Force Geophysics Laboratory, 1986.

P. Debye. *Polar Molecules.* Dover, New York, 1929.

B. Edlén. The refractive index of air. *Metrologia*, 2(2):71–80, 1966. doi:10.1088/0026-1394/2/2/002.

G. Elgered. Tropospheric radio-path delay from ground based microwave radiometry. In M. Janssen, editor, *Atmospheric Remote Sensing by Microwave Radiometry*, chapter 5. Wiley & Sons, Inc., N.Y., 1993.

G. Elgered, J. L. Davis, T. A. Herring, and I. I. Shapiro. Geodesy by radio interferometry: Water vapor radiometry for estimation of the wet delay. *J. Geophys. Res.*, 95(B4):6541–6555, 1991. doi:10.1029/90JB00834.

G. Elgered, H.-P. Plag, H. van der Marel, S. Barlag, and J. Nash, editors. *Exploitation of ground-based GPS for operational numerical weather prediction and climate applications*. COST action 716: Final Report. European Union, Brussels, Belgium, 2005.

T. R. Emardson and H. J. P. Derks. On the relation between the wet delay and the integrated precipitable water vapour in the European atmosphere. *Meteorol. Appl.*, 7(1):61–68, 2000. doi:10.1017/S1350482700001377.

T. R. Emardson, G. Elgered, and J. M. Johansson. External atmospheric corrections in geodetic very-long-baseline interferometry. *J. Geodesy*, 73:375–383, 1999. doi:10.1007/s001900050256.

L. Essen and K. D. Froome. The refractive indices and dielectric constants of air and its principal constituents at 24,000 Mc/s. *Proc. Phys Soc.* B, 64(10):862–875, 1951. doi:10.1088/0370-1301/64/10/303.

A. Flores, G. Ruffini, and A. Rius. 4D tropospheric tomography using GPS slant delays. *Ann. Geophysicae*, pages 223–234, 2000. doi:10.1007/s00585-000-0223-7.

U. Fölsche. *Tropospheric water vapor imaging by combination of spaceborne and ground-based GNSS sounding data*. PhD thesis, Univ. Graz, Graz, Austria, 1999.

P. J. Fowler. Finite-difference solutions of the 3d eikonal equation in spherical coordinates. In *Proc. 64th SEG meeting*, pages 1394–1397, Los Angeles, USA, 1994.

C. S. Gardner. Effects of horizontal refractivity gradients on the accuracy of laser ranging to satellites. *Radio Sci.*, 11(12):1037–1044, 1976. doi:10.1029/RS011i012p01037.

P. Gegout, R. Biancale, and L. Soudarin. Adaptive mapping functions to the azimuthal anisotropy of the neutral-atmosphere. *J. Geodesy*, 85(10):661–677, 2011. doi:10.1007/s00190-011-0474-y.

L. Gradinarsky and P. Jarlemark. Ground-based GPS tomography of water vapor: Analysis of simulated and real data. *J. Meteorol. Soc. Japan*, 82:551–560, 2004. doi:10.2151/jmsj.2004.551.

L. P. Gradinarsky, J. M. Johansson, H. R. Bouma, H.-G. Scherneck, and G. Elgered. Climate monitoring using GPS. *Physics and Chemistry of the Earth*, 27:335–340, 2002. doi:10.1016/S1474-7065(02)00009-8.

B. A. Greene and T. A. Herring. Multiple wavelength laser ranging. In *The 6th International Workshop on Laser Ranging Instrumentation*, 1986.

S. I. Gutman and S. G. Benjamin. The role of ground-based GPS meteorological observations in numerical weather prediction. *GPS Solutions*, 4(4):16–24, 2001. doi:10.1007/PL00012860.

R. Heinkelmann, J. Böhm, H. Schuh, S. Bolotin, G. Engelhardt, D. S. MacMillan, M. Negusini, E. Skurikhina, V. Tesmer, and O. Titov. Combination of long time-series of troposphere zenith delays observed by VLBI. *J. Geodesy,* 81(6–8):483–501, 2007. doi:10.1007/s00190-007-0147-z.

T. A. Herring. Modeling atmospheric delays in the analysis of space geodetic data. In J.C. De Munk and T. A. Spoelstra, editors, *Symposium on Refraction of Transatmospheric Signals in Geodesy*, pages 157–164. Netherlands Geod. Comm., Delft, 1992.

T. A. Herring, J. L. Davis, and I. I. Shapiro. Geodesy by radio interferometry: The application of Kalman filtering to the analysis of Very Long Baseline Interferometry data. *J. Geophys. Res.*, 95(B8):12,561–12,581, 1990. 90JB00683.

R. J. Hill, R. S. Lawrence, and J. T. Priestley. Theoretical and calculational aspects of the radio refractive index of water vapor. *Radio Sci.*, 17(5):1251–1257, 1982. doi:10.1029/RS017i005p01251.

T. Hobiger, R. Ichikawa, Y. Koyama, and T. Kondo. Fast and accurate ray-tracing algorithms for real-time space geodetic applications using numerical weather models. *J. Geophys. Res.*, 113:D20302, 2008. doi:10.1029/2008JD010503.

H.S. Hopfield. Two-quartic tropospheric refractivity profile for correcting satellite data. *J. Geophys. Res.*, 74:4487–4499, 1969. doi:10.1029/JC074i018p04487.

C. G. Hulley. *Improved Refraction Corrections for Satellite Laser Ranging (SLR) by Ray Tracing through Meteorological Data*. PhD thesis, University of Maryland, 2007.

G. C. Hulley and E. C. Pavlis. A ray-tracing technique for improving Satellite Laser Ranging atmospheric delay corrections, including the effects of horizontal refractivity gradients. *J. Geophys. Res.*, 112(B06417):1–19, 2007. doi:10.1029/2006JB004834.

I. Ifadis. The atmospheric delay of radio waves: Modeling the elevation dependence on a global scale. Technical Report 38L, School Electrical Computer Engineering, Chalmers University of Technology, Göteborg, Sweden, 1986. ISBN:99-0605353-4.

K. Iizuka. Engineering optics, volume 35 of *Springer Series in Optical Sciences*. Springer-Verlag, New York, 3rd edition, 2008.

A. Ishimaru. *Wave Propagation and Scattering in Random Media*. Academic Press, New York, 1978.

J. D. Jackson. *Classical electrodynamics*. Wiley & Sons, Inc., N.Y., 3rd edition, 1998.

P. O. J. Jarlemark. Analysis of temporal and spatial variations in atmospheric water vapor using microwave radiometry. PhD Thesis, Tech. Rep. 308, School Electrical Computer Engineering, Chalmers Univ. Tech., 1997. Göteborg, Sweden.

H. Jeske. Meteorological optics and radiometeorology. In Landolt-Börnstein, editor, *Numerical data and functional relationships in science and technology*, volume 4b of Group V. Springer, 1988.

S. Jin, J.-U. Park, J.-H. Cho, and P.-H. Park. Seasonal variability of GPS-derived zenith tropospheric delay (1994–2006) and climate implications. *J. Geophys. Res.*, 112:D09110, 2007. doi:10.1029/2006JD007772.

A. Karabatić, R. Weber, and T. Haiden. Near real-time estimation of tropospheric water vapour content from ground based GNSS data and its potential contribution to weather now-casting in Austria. *Adv. Space Res.*, 47(10):1691–1703, 2011. doi:10.1016/j.asr.2010.10.028.

A. N. Kolmogorov. Dissipation of energy in the locally isotropic turbulence. *Dokl. Akad. Nauk SSSR*, 32(1):16–18, 1941a. English translation in: *Proc R. Soc. Lond. A*, 434:15–17.

A. N. Kolmogorov. The local structure of turbulence in incompressible viscous fluid for very large Reynolds numbers. *Dokl. Akad. Nauk SSSR*, 30(4):299–303, 1941b. English translation in: *Proc R. Soc. Lond. A*, 434:9–13.

J. Kouba. Implementation and testing of the gridded vienna mapping function 1 (VMF1). *J. Geodesy*, 82(4–5):193–205, 2008. doi:10.1007/s00190-007-0170-0.

C. E. Kuehn, W. E. Himwich, T. A. Clark, and C. Ma. An evaluation of water vapor radiometer data for calibration of the wet path delay in very long baseline interferometry experiments. *Radio Sci.*, 26(6):1381–1391, 1991. doi:10.1029/91RS02020.

R.F. Leandro, M.C. Santos, and R.B. Langley. UNB neutral atmosphere models: Development and performance. In *National Technical Meeting of The Institute of Navigation, Monterey, California, 18–20 January 2006*, pages 564–573, 2006.

H. J. Liebe. An updated model for millimeter wave propagation in moist air. *Radio Sci.*, 20(5): 1069–1089, 1985. doi:10.1029/RS020i005p0106.

H. J. Liebe. MPMan atmospheric millimeter-wave propagation model. *Int. J. Infrared Millimeter Waves*, 10(6): 631–650, 1989. doi:10.1007/BF01009565.

H. J. Liebe, G. A. Hufford, and M. G. Cotton. Propagation modeling of moist air and suspended water/ice particles at frequencies below 1000 GHz. In *Proc. AGARD 52d Specialists Meeting of the Electromagnetic Wave Propagation Panel, pages 3.1–3.10, Palam de Mallorca*, Spain, 1993. AGARD.

D. S. MacMillan. Atmospheric gradients from very long baseline interferometry observations. *Geophys. Res. Lett.*, 22(9):1041–1044, 1995. doi:10.1029/95GL00887.

D. S. MacMillan and C. Ma. Evaluation of very long baseline interferometry atmospheric modeling improvements. *J. Geophys. Res.*, 99(B1):637–651, 1994. doi:10.1029/93JB02162.

D. S. MacMillan and C. Ma. Atmospheric gradients and the VLBI terrestrial and celestial reference frames. *Geophys. Res. Lett.*, 24(4):453–456, 1997. doi:10.1029/97GL00143.

J.W. Marini. Correction of satellite tracking data for an arbitrary tropospheric profile. *Radio Science*, 7(2):223–231, 1972. doi:10.1029/RS007i002p00223.

J.W. Marini and C.W. Murray. Correction of laser range tracking data for atmospheric refraction at elevation angles above 10 degrees. Technical Report X-591-73-351, NASA, 1973.

V. B. Mendes. Modeling of the neutral-atmosphere propagation delay in radiometric space techniques. PhD dissertation, Department of Geodesy and Geomatics Engineering Tech. Report No. 199, University of New Brunswick, Fredericton, New Brunswick, Canada, 1999. General definitions of IWV, relative humidity etc.

V. B. Mendes and R. Langley. Tropospheric zenith delay prediction accuracy for airborne GPS high-precision positioning. In *Proc. of* ION GPS-98, pages 337–347, Nashville, TN, USA, 1998.

V. B. Mendes and E. C. Pavlis. High-accuracy zenith delay prediction at optical wavelengths. *Geophys. Res. Lett.*, 31, 2004. doi:10.1029/2004GL020308.L14602.

V. B. Mendes, G. Prates, E. C. Pavlis, D. E. Pavlis, and R. B. Langley. Improved mapping functions for atmospheric refraction correction in SLR. *Geophys. Res. Lett.*, 29(10):10.1029-10.1032, 2002. doi:10.1029/2001GL014394.

V. Nafisi, M. Madzak, J. Böhm, A. A. Ardalan, and H. Schuh. Ray-traced tropospheric delays in VLBI analysis. *Radio Sci.*, 47:RS2020, 2012a. doi:10.1029/2011RS004918.

V. Nafisi, L. Urquhart, M. C. Santos, F. G. Nievinski, J. Böhm, D. D. Wijaya, H. Schuh, A. A. Ardalan, T. Hobiger, R. Ichikawa, F. Zus, J. Wickert, and P. Gegout. Comparison of ray-tracing packages for troposphere delays. *IEEE Trans. Geosci. Remote Sensing*, 50(2):469–481, 2012b. doi:10.1109/TGRS.2011.2160952.

A. Niell. Global mapping functions for the atmosphere delay at radio wavelengths. *J. Geophys. Res.*, 101(B2):3227–3246, 1996. doi:10.1029/95JB03048.

A. E. Niell. Improved atmospheric mapping functions for VLBI and GPS. *Earth Planets Space*, 52:699–702, 2000.

A. E. Niell. Preliminary evaluation of atmospheric mapping functions based on numerical weather models. *Phys. Chem. Earth (A)*, 26:475–480, 2001. doi:10.1016/S1464-1895(01)00087-4.

A. E. Niell, A. J. Coster, F. S. Solheim, V. B. Mendes, P. C. Toor, R. B. Langley, and C. A. Upham. Comparison of measurements of atmospheric wet delay by Radiosonde, Water Vapor Radiometer, GPS, and VLBI. *J. Atmos. Oceanic Technol.*, 18(6):830–850, 2001. doi:10.1175/1520-0426(2001)018<0830:COMOAW>2.0.CO;2.

A. E. Niell. Interaction of atmosphere modeling and vlbi analysis strategy. In D. Behrend and K. Baver, editors, *International VLBI Service for Geodesy and Astrometry 2006 General Meeting Proceedings*, number NASA/CP-2006-214140, 2006.

F. G. Nievinski. Ray-tracing options to mitigate the neutral atmosphere delay in GPS. Master's thesis, University of New Brunswick, Department of Geodesy and Geomatics Engineering, 2009. URL http://hdl.handle.net/1882/1050. Technical Report No. 262.

T. Nilsson. Improving GNSS tropospheric tomography by better knowledge of atmospheric turbulence. In *Proc. 1:st Colloquium Scientific and Fundamental Aspects of the Galileo Programme*, Toulouse, France, 2007. European Space Agency.

T. Nilsson and G. Elgered. Long-term trends in the atmospheric water vapor content estimated from ground-based GPS data. *J. Geophys. Res.*, 113:D19101, 2008. doi:10.1029/2008JD010110.

T. Nilsson and L. Gradinarsky. Water vapor tomography using GPS phase observations: Simulaton results. *IEEE Trans. Geosci. Remote Sensing*, 44(10):2927–2941, 2006. doi:10.1109/TGRS.2006.877755.

T. Nilsson, L. Gradinarsky, and G. Elgered. Correlations between slant wet delays measured by microwave radiometry. *IEEE Trans. Geosci. Remote Sensing*, 43(5):1028–1035, 2005. doi:10.1109/TGRS.2004.840659.

T. Nilsson, L. Gradinarsky, and G. Elgered. Water vapour tomography using GPS phase observations: Results from the ESCOMPTE experiment. *Tellus A*, 59:574–682, 2007. doi:10.1111/j.1600-0870.2007.00247.x.

T. Nilsson and R. Haas. Impact of atmospheric turbulence on geodetic very long baseline interferometry. *J. Geophys. Res.*, 115:B03407, 2010. doi:10.1029/2009JB006579.

T. Ning and G. Elgered. Trends in the atmospheric water vapor content from ground-based GPS: The impact of the elevation cutoff angle. *IEEE Journal of Selected Topics in Applied Earth Observations and Remote Sensing*, 5:744–751, 2012. doi:10.1109/JSTARS.2012.2191392.

A. Nothnagel, J. Cho, A. Roy, and R. Haas. WVR calibration applied to European VLBI observing sessions. In P. Tregoning and C. Rizos, editors, *Dynamic Planet*, volume 130 of *IAG Symposia*, pages 152–157. Springer, Berlin, Germany, 2007. doi:10.1007/978-3-540-49350-1_24.

J. C. Owens. Optical refractive index of air: Dependence on pressure, temperature and composition. *Appl. Opt.*, 6(1):51–59, 1967. doi:10.1364/AO.6.000051.

T. K. Pany. *Development and application of tropospheric GPS slant delay models based on numerical weather prediction models and turbulence theory*. PhD thesis, Institute of Engineering Geodesy and Measurements Systems, Graz University of Technology, 2002.

D. Perler, A. Geiger, and F. Hurter. 4D GPS water vapor tomography: new parameterized approaches. *J. Geodesy*, 85(8):539–550, 2011. doi:10.1007/s00190-011-0454-2.

P. Poli, P. Moll, F. Rabier, G. Desroziers, B. Chapnik, L. Berre, S. B. Healy, E. Andersson, and F.-Z. El Guelai. Forecast impact studies of zenith total delay data from European near real-time GPS stations in météo france 4DVAR. *J. Geophys. Res.*, 112:D06114, 2007. doi:10.1029/2006JD007430.

M. T. Prilepin. Light modulating method for determining average index of refraction of air along a line. *Tr. Tsentr. Nauchno-Issled. Inst. Geod. Aero. Kartog.*, 114:127, 1957.

L. F. Richardson. The supply of energy from and to atmospheric eddies. *Proc. Roy. Soc. Lond. A*, 97(686):354–373, 1920.

P. W. Rosenkranz. Water vapor microwave continuum absorption: a comparison of measurements and models. *Radio Sci.*, 33(4):919–928, 1998. doi:10.1029/98RS01182.

M. Rothacher, T.A. Springer, S. Schaer, and G. Beutler. Processing strategies for regional GPS networks. In F.K. Brunner, editor, *Advances in Positioning and Reference Frames, volume 118 of IAG Symposia Series*, pages 93–100. Springer-Verlag, 1998.

J. M. Rüeger. Refractive index formulae for radio waves. In *Proc. XXII FIG International Congress*, Washington DC, USA, 2002a. FIG. URL http://www.fig.net/pub/fig_2002/procmain.htm

J. M. Rüeger. Refractive indices of light, infrared and radio waves in the atmosphere. Technical report, UNISURV S-68, School of Surveying and Spatial Information Systems, The University of New South Wales, Australia, 2002b.

J. Saastamoinen. Atmospheric correction for the troposphere and stratosphere in radio ranging of satellites. In S. W. Henriksen et al., editors, *The Use of Artificial Satellites for Geodesy*, volume 15, pages 247–251, AGU, Washington, D.C., 1972b.

J. Saastamoinen. Introduction to practical computation of astronomical refraction. *Bull. Géod.*, 106:383–397, 1972a. doi:10.1007/BF02522047.

T. M. Scheve and C. T. Swift. Profiling atmospheric water vapor with a K-band spectral radiometer. *IEEE Trans. Geosci.* Remote Sensing, 37(3):1719–1729, 1999. doi:10.1109/36.763294.

W. A. Schneider, Jr. Robust, efficient upwind finite-difference traveltime calculations in 3d. In *Proc. 63rd SEG meeting*, pages 1036–1039, Washington, DC, USA, 1993.

S. D. Schubert, J. Pjaendtner, and R. Rood. An assimilated data set for earth science applications. *Bull. American. Meteo. Soc.*, 74:2331–2342, 1993. doi:10.1175/1520-0477(1993)074<2331:AADFES>2.0.CO;2.

K. Snajdrova, J. Böhm, P. Willis, R. Haas, and H. Schuh. Multi-technique comparison of tropospheric zenith delays derived during the CONT02 campaign. *J. Geodesy,* 79(10–11):613–623, 2006. doi:10.1007/s00190-005-0010-z.

F. S. Solheim, J. Vivekanandan, R. H. Ware, and C. Rocken. Propagation delays induced in GPS signals by dry air, water vapor, hydrometeors, and other particulates. *J. Geophys. Res.*, 104(D8):9663–9670, 1999. doi:10.1029/1999JD900095.

P. Steigenberger, J. Böhm, and V. Tesmer. Comparison of GMF/GPT with VMF1/ECMWF and implications for atmospheric loading. *J. Geodesy*, 83:943–951, 2009. doi:10.1007/s00190-009-0311-8.

P. Steigenberger, V. Tesmer, M. Krügel, D. Thaller, R. Schmid, S. Vey, and M. Rothacher. Comparisons of homogeneously reprocessed GPS and VLBI long time-series of troposphere zenith delays and gradients. *J. Geodesy*, 81(6–8):503–514, 2007. doi:10.1007/s00190-006-0124-y.

V. I. Tatarskii. *The Effects of the Turbulent Atmosphere on Wave Propagation*. Israel Program for Scientific Translations, Jerusalem, 1971.

G. I. Taylor. The spectrum of turbulence. *Proc. Roy. Soc. Lond. A*, 164(919):476–490, 1938. URL http://www.jstor.org/stable/97077.

K. Teke, J. Böhm, T. Nilsson, H. Schuh, P. Steigenberger, R. Dach, R. Heinkelmann, P. Willis, R. Haas, S. Garcia-Espada, T. Hobiger, R. Ichikawa, and S. Shimizu. Multi-technique comparison of troposphere zenith delays and gradients during CONT08. *J. Geodesy*, 85(7):395–413, 2011. doi:10.1007/s00190-010-0434-y.

V. Tesmer, J. Böhm, R. Heinkelmann, and H. Schuh. Effect of different tropospheric mapping functions on the TRF, CRF and position time-series estimated from VLBI. *J. Geodesy*, 81(6–8): 409–421, 2007. doi:10.1007/s00190-006-0126-9.

G. D. Thayer. A rapid and accurate ray tracing algorithm for a horizontally stratified atmosphere. *Radio Sci.*, 1(2):249–252, 1967.

G. D. Thayer. An improved equation for the radio refractive index of air. *Radio Sci.*, 9(10):803–807, 1974. doi:10.1029/RS009i010p00803.

R. N. Thessin. Atmospheric signal delay affecting GPS measurements made by space vehicles during launch, orbit and reentry. Master's thesis, Massachusetts Institute of Technology, Dept. of Aeronautics and Astronautics, Cambridge, Mass., 2005. URL http://hdl.handle.net/1721.1/33211.

D. M. Tralli and S. M. Lichten. Stochastic estimation of tropospheric path delays in global positioning system geodetic measurements. *Bull. Geod.*, 64:127–159, 1990. doi:10.1007/BF02520642.

P. Tregoning and T.A. Herring. Impact of a priori zenith hydrostatic delay errors on GPS estimates of station heights and zenith total delays. *Geophys. Res. Lett.*, 33(L23303), 2006. doi:10.1029/2006GL027706.

K. E. Trenberth, A. Dai, R.M. Rasmussen, and D.B. Parsons. The changing character of precipitation. *Bull. Amer. Meteor. Soc.*, 84(9):12051217, 2003. doi:10.1175/BAMS-84-9-1205.

R. N. Treuhaft and G. E. Lanyi. The effect of the dynamic wet troposphere on radio interferometric measurements. *Radio Sci*., 22(2):251–265, 1987. doi:10.1029/RS022i002p00251.

M. Troller, A. Geiger, E. Brockmann, J.-M. Bettems, B. Bürki, and H.-G. Kahle. Tomographic determination of the spatial distribution of water vapor using GPS observations. *Adv. Space Res.*, 37(12):2211–2217, 2006. doi:10.1016/j.asr.2005.07.002.

H. Vedel. Targeting optimal use of GPS humidity measurements in meteorology: Final report of the TOUGH project, 2006. URL http://web.dmi.dk/pub/tough/.

H. Vedel and X.-Y. Huang. Impact of ground based GPS data on numerical weather prediction. *J. Met. Soc. Japan*, 82(1B):459–472, 2004. doi:10.2151/jmsj.2004.459.

J. Wang, L. Zhang, and A. Dai. Global estimates of water-vapor-weighted mean temperature of the atmosphere for GPS applications. *J. Geophys. Res.*, 110(D21101), 2005. doi:10.1029/2005JD006215.

R. Ware, C. Rocken, F. Solheim, T. van Hove, C. Alber, and J. Johnson. Pointed water vapor radiometer corrections for accurate global positioning system surveying. *Geophys. Res. Lett.*, 20(23): 2635–2638, 1993. doi:10.1029/93GL02936.

E. R. Westwater, M. J. Falls, and I. A. Popa-Fotin. Ground-based microwave radiometric observations of precipitable water vapor: A comparison with ground truth from two radiosonde observing systems. *J. Atmos. Oceanic Technol.*, 6(4):724–730, 1989. doi:10.1175/1520-0426(1989)006.

A. D. Wheelon. *Electromagnetic scintillation: Geometrical optics*. Cambridge University Press, 2001.

D. D. Wijaya. *Atmospheric correction formulae for space geodetic techniques*. PhD thesis, Graz University of Technology, Institute of Engineering Geodesy and Measurements Systems, Graz, Austria, 2010.

D. D. Wijaya, J. Böhm, M. Karbon, and H. Schuh. Atmospheric pressure loading. In *Atmospheric Effects in Space Geodesy*. Springer-Verlag, 2013. this book.

D.D. Wijaya and F.K. Brunner. Atmospheric range correction for two-frequency SLR measurements. *J. Geodesy*, 85(9):623–635, 2011. doi:10.1007/s00190-011-0469-8.

S.-C. Wu. Optimum frequencies of a passive microwave radiometer for tropospheric path-length correction. *IEEE Trans. Antennas Propagat.*, 27:233–239, 1979. doi:10.1109/TAP.1979.1142066.